Quantification of the dust optical depth across spatiotemporal scales with the MIDAS global dataset (2003-2017)

Antonis Gkikas[1], Emmanouil Proestakis[1], Vassilis Amiridis[1], Stelios Kazadzis[2,3], Enza Di Tomaso[4], Eleni Marinou[1,5], Nikos Hatzianastassiou[6], Jasper F. Kok[7] and Carlos Pérez García-Pando[4,8]

[1]Institute for Astronomy, Astrophysics, Space Applications and Remote Sensing, National Observatory of Athens, Athens, 15236, Greece
[2]Physikalisch-Meteorologisches Observatorium Davos, World Radiation Center, Switzerland
[3]Institute of Environmental Research and Sustainable Development, National Observatory of Athens, Greece
[4]Barcelona Supercomputing Center, Barcelona, Spain
[5]Deutsches Zentrum für Luft- und Raumfahrt (DLR), Institut für Physik der Atmosphäre, Oberpfaffenhofen, Germany
[6]Laboratory of Meteorology, Department of Physics, University of Ioannina, Ioannina, Greece
[7]Department of Atmospheric and Oceanic Sciences, University of California, Los Angeles, CA 90095, USA
[8]ICREA, Catalan Institution for Research and Advanced Studies, Barcelona, Spain

Corresponding author: Antonis Gkikas (agkikas@noa.gr)

Abstract

Quantifying the dust optical depth (DOD) and its uncertainty across spatiotemporal scales is key to understanding and constraining the dust cycle and its interactions with the Earth System. This study quantifies the DOD along with its monthly and year-to-year variability between 2003 and 2017 at global and regional levels based on the MIDAS (ModIs Dust AeroSol) dataset, which combines MODIS-Aqua retrievals and MERRA-2 reanalysis products. We also describe the annual and seasonal geographical distributions of DOD across the main dust source regions and transport pathways. MIDAS provides columnar mid-visible (550 nm) DOD at fine spatial resolution (0.1° x 0.1°), expanding the current observational capabilities for monitoring the highly variable spatiotemporal features of the dust burden. We obtain a global DOD of 0.032 ± 0.003 – approximately a quarter ($23.4\% \pm 2.4\%$) of the global AOD – with about one order of magnitude more DOD in the northern hemisphere (0.056 ± 0.004; $31.8\% \pm 2.7\%$) than in the southern hemisphere (0.008 ± 0.001; $8.2\% \pm 1.1\%$) and about 3.5 times more DOD over land (0.070 ± 0.005) than over ocean (0.019 ± 0.002). The northern hemisphere monthly DOD is highly correlated with the corresponding monthly AOD ($R^2=0.94$) and contributes 20% to 48% of it, both indicating a dominant dust contribution. In contrast, the contribution of dust to the monthly AOD does not exceed 17% in the southern hemisphere, although the uncertainty in this region is larger. Among the major dust sources of the planet, the maximum DODs (~1.2) are recorded in the Bodélé Depression of the northern Lake Chad

38   Basin, whereas moderate-to-high intensities are encountered in the Western Sahara (boreal summer),

39   along the eastern parts of the Middle East (boreal summer) and in the Taklamakan Desert (spring).

40   Over oceans, major long-range dust transport is observed primarily along the Tropical Atlantic

41   (intensified during boreal summer) and secondarily in the North Pacific (intensified during boreal

42   spring). Our calculated global and regional averages and associated uncertainties are consistent with

43   some but not all recent observationally based studies. Our work provides a simple, yet flexible method

44   to estimate consistent uncertainties across spatiotemporal scales, which will enhance the use of the

45   MIDAS dataset in a variety of future studies.

47   **1. Introduction**

48   Mineral dust particles are emitted throughout the year across the arid and semi-arid regions of the

49   planet, when winds exceed a threshold velocity mainly determined by soil texture, soil moisture, and

50   surface roughness. While dust aerosols have mainly a natural origin, the contribution of

51   anthropogenic land use is estimated to be between 10% and 25 % (Tegen et al. 2004; Stanelle et al.,

52   2014; Ginoux et al., 2012). Dust is mobilized by microscale to synoptic scale phenomena, from dust

53   devils developed under strong surface heating (Koch and Renno, 2005), to "haboobs" formed by

54   intense cold-pool downdrafts related to deep moist convection (Knippertz et al., 2007), to synoptic

55   patterns associated with intensified pressure gradients (Klose et al., 2010) and low-level jets (LLJ;

56   Fiedler et al., 2013). Meteorology also plays a key role in the dust transport over maritime areas taking

57   place mainly across the Tropical Atlantic Ocean (Prospero and Mayol-Bracero, 2013; Yu et al., 2015),

58   the northern Pacific Ocean (Husar et al., 2001), the Mediterranean (Flaounas et al., 2015; Gkikas et

59   al., 2015), the Arabian Sea (Ramaswamy et al., 2017) and the southern Atlantic Ocean (Gasso and

60   Stein, 2007). Dust perturbs the radiation budget through direct (Sokolik and Toon, 1996), semi-direct

61   (Huang et al., 2006) and indirect (Haywood and Bucher, 2000) processes, leading to impacts upon

62   weather (Pérez et al., 2006; Gkikas et al., 2018; Gkikas et al., 2019) and climate (Lambert et al., 2013;

63   Nabat et al., 2015). Upon deposition, nutrient-rich dust particles can increase the productivity of

64   oceanic waters (Jickells et al., 2005) and terrestrial ecosystems (Okin et al., 2004) and perturb the

65   carbon cycle (Jickells et al., 2014). Dust has been associated with epidemics of meningococcal

66   meningitis in the African Sahel (Pérez García-Pando et al., 2014a, b) and with air quality degradation

67   in urban areas (Kanakidou et al., 2011) causing respiratory (Kanatani et al., 2010) and cardiovascular

68   (Du et al., 2016) disease when the population is exposed to high dust concentrations (Querol et al.,

69   2019). Other socio-economic sectors can be regionally affected by dust storms (Middleton, 2017),

70   including transportation (Weinzierl et al., 2012), agriculture (Stefanski and Sivakumar, 2009) and

71   solar energy production (Kosmopoulos et al., 2018).

Satellite measurements and numerical simulations have repeatedly shown the remarkable contrast in dust load between the two hemispheres. The substantially higher dust load in the N. Hemisphere is associated to the wider deserts extending across the so-called "dust belt" (Prospero et al., 2002; Ginoux et al., 2012) in contrast to the smaller sources in Australia, South Africa and South America. At global scale, most of the entrained dust loads in the atmosphere originate from tropical and sub-tropical arid regions; yet, it is estimated that up to 5% of the global dust budget consists of particles emitted from high-latitude sources (Bullard and Austin, 2011; Bullard et al., 2016). Given the key role of dust aerosols in the Earth system it is imperative to monitor and understand the global dust cycle along with its multi-scale spatiotemporal variability over long time periods and fine spatial resolution. This task can be fulfilled to a certain degree using contemporary satellite instruments providing accurate retrievals and global coverage over extended time periods. With this approach, one of the key challenges is to discriminate dust from other aerosols. Several studies have combined AOD and aerosol index (AI) (e.g., Middleton and Goudie, 2001; Prospero et al., 2002) or AOD, single scattering albedo (SSA) and Ångström exponent (AE) (Ginoux et al., 2012) to identify the most active dust sources worldwide. Other studies have focused on the dust load and its variability in specific regions such as the Atlantic Ocean and the Arabian Sea (Peyridieu et al., 2013), the Sistan basin (Rashki et al., 2015), the Mediterranean (Gkikas et al., 2016), Europe and North Africa (Marinou et al., 2017) and east Asia (Proestakis et al., 2018), among others. Liu et al. (2008) described the three-dimensional structure of dust aerosols at global scale based on CALIOP vertically resolved retrievals acquired during the first operational year of the CALIPSO satellite mission. A more advanced approach has been introduced by Amiridis et al. (2013) and Marinou et al. (2017), who applied a more realistic lidar ratio for the Saharan dust and a series of quality filters on the CALIOP vertical profiles, in order to provide information about the vertical structure of dust layers at global scale and coarse resolution in the LIVAS dataset (Amiridis et al., 2015). Ridley et al. (2016) quantified the global average DOD and its uncertainty for the period 2004-2008 based on AOD retrievals from passive spaceborne sensors (MODIS, MISR), ground-based (AERONET) and shipborne (MAN) measurements from sun-photometers, and numerical simulations. Voss and Evan (2020) provided a long-term DOD climatology over the Tropics and mid-latitudes at a coarse spatial resolution ($1° \times 1°$) based on MODIS and AVHRR observations, where DOD was estimated based on AOD, SSA and AE over land following Ginoux et al. (2012) and AOD, fine and coarse AOD (AERONET) and MERRA-2 winds over ocean. Based on vertically-resolved CALIOP retrievals and columnar MODIS optical properties, Song et al. (2021) provided a long-term 4D global dust optical depth dataset, excluding the polar regions, over the period 2007 – 2019. In their approach, they took advantage of spaceborne observations that can be used for the discrimination/identification of dust aerosols characterized by their aspherical shape, coarse size and absorption.

107   Our study provides a global and regional quantification and description of the DOD based on the
108 new ModIs Dust AeroSol (MIDAS) dataset (Gkikas et al., 2021). The powerful and innovative
109 elements of the MIDAS DOD dataset are the: (i) daily availability and fine spatial resolution (0.1° x
110 0.1°), (ii) full global coverage including the sources and downwind areas (both over land and sea),
111 (iii) 15-year temporal range (2003 – 2017) using the most updated MODIS data collection, (iv) grid-
112 cell level uncertainty quantification. In this contribution, we first describe the annual and seasonal
113 geographical distribution of DOD across the main dust source regions and transport pathways
114 (Section 4.1). We then quantify the average DOD and its monthly and year-to-year variability at
115 global, hemispherical and regional levels, along with its fractional contribution to the AOD (Section
116 4.2). We summarize the main findings in Section 5.

117 **2. ModIs Dust AeroSol (MIDAS) dataset**
118   Our study is based on the MIDAS global fine resolution dataset described in detail in Gkikas et
119 al. (2021). We analyse the DOD at 550 nm at 0.1° x 0.1° spatial resolution between 2003 to 2017.
120 The MIDAS DOD results from the combination of the quality-filtered MODIS aerosol optical depth
121 (AOD, Collection 6.1, Level 2; Levy et al., 2013) and the MERRA-2 (Modern-Era Retrospective
122 Analysis for Research and Applications, version 2; Gelaro et al., 2017) fraction of AOD that is due
123 to dust (MDF). In Gkikas et al. (2021), the MDF was evaluated against the dust fraction obtained
124 from quality-assured dust and non-dust CALIOP (Cloud-Aerosol Lidar with Orthogonal Polarization;
125 Winker et al., 2009) profiles, available from the LIVAS database (Amiridis et al., 2015; Marinou et
126 al., 2017; Proestakis et al., 2018). The MDF compares well with the LIVAS dust fraction over the
127 dust-abundant areas extending across the NH dust belt, with maximum underestimations of 10 % in
128 Asian deserts. The agreement is more limited in North America and the Southern Hemisphere
129 (Figures 1 and 2 in Gkikas et al., 2021). Overall, the MIDAS DOD is well correlated with AERONET
130 dust-dominant retrievals (R=0.89 at global scale) and the absolute biases are mainly below 0.12 at
131 stations near sources (Figures 3 and 4 in Gkikas et al., 2021). The MIDAS DOD dataset was further
132 verified against the LIVAS DOD and compared with MERRA-2 DODs (Figure 5 in Gkikas et al.,
133 2021). Among the three datasets, there is good agreement on the monthly variability of the global and
134 hemispherical DODs as well as on their long-term averages (Figure 6 and Table 1 in Gkikas et al.,
135 2021). Moreover, the annual and seasonal DOD patterns are broadly similar in the three datasets
136 throughout the period 2007 – 2015. Nevertheless, regionally differences are found due to the different
137 techniques (passive and active remote sensing, numerical simulations) applied for the DOD
138 derivation.
139
140

141 **3. Spatiotemporal averaging and propagation of grid-cell level uncertainties**

142   In section 4.2 we provide DOD estimates that are averaged in space (regionally and globally) and
143 in time (over months, seasons and years) along with their respective uncertainties. Averaging is
144 performed according to the upper branch of Figure 5 in Levy et al. (2009), i.e. spatial averaging is
145 performed after grid cell temporal averaging for any of the timescales considered. The uncertainties
146 of the DOD averages at the different spatiotemporal scales are based on the propagation of the daily
147 grid cell uncertainties provided within the MIDAS dataset and presented in Gkikas et al. (2021). In
148 short, the daily grid cell uncertainties combine the uncertainties of the MODIS AOD and the
149 MERRA-2 MDF with respect to AERONET and LIVAS, respectively. The former is based on linear
150 equations expressing the uncertainty with respect to AERONET AOD over ocean (Levy et al., 2013)
151 and land (Levy et al., 2010; Sayer et al. 2013) with updated coefficients for C061 data depending on
152 vegetated and arid surface types (see equations 4 to 7 in Gkikas et al., 2021). The latter is based on a
153 quartic (fourth degree) polynomial equation expressing the uncertainty with respect to the LIVAS
154 dust fraction (see equation 8 in Gkikas et al., 2021).

155   In order to estimate the uncertainties of the spatiotemporal averages we first assume that each of
156 the daily grid cell uncertainties are composed of (1) a fraction that is completely random in time and
157 space, (2) a fraction that is systematic (correlated) in time and random in space and (3) a fraction that
158 is systematic (correlated) in space and random in time. Our framework also assumes that the fraction
159 of the daily grid cell uncertainty that is correlated both in space and time, for instance an instrument
160 bias, is very small and therefore neglected. Under this framework, the propagation of uncertainty
161 fraction (1) is negligible across the spatiotemporal scales considered, the propagation of uncertainty
162 fraction (2) depends upon the size of the domain considered but is negligible at global scale and across
163 most of the regional domains considered in this study, and propagation of fraction (3) accounts for
164 most of the total average uncertainty. Since we cannot know fractions (1), (2) and (3) and (1) and (2)
165 are negligible or small, we assume that (3) represents 100 % of the uncertainty, i.e the grid cell
166 uncertainty is systematic (correlated) in space and random in time, to provide an upper limit on the
167 uncertainty. In addition, we also take into account the sampling uncertainty when temporally
168 averaging over each grid cell using the standard error, i.e., we take the standard deviation divided by
169 the square root of the number of measurements.

170   In practice, when averaging the daily values for every grid cell i over months, seasons, or years,
171 the uncertainty σ'_i is obtained by adding in quadrature the daily uncertainties $\sigma^2_{N_i}$ and dividing by the
172 number of available daily measurements N_i:

173
$$\sigma'_i = \frac{\sqrt{\sigma^2_{i,1} + \sigma^2_{i,2} + \cdots + \sigma^2_{N_i}}}{N_i} \textbf{ (Eq. 1)}$$

174

175   In addition, we add in quadrature σ'_i and the standard error SE_i to obtain the total uncertainty of

176   the temporal average σ_i for every grid cell:

177

178
$$\sigma_i = \sqrt{\sigma'^2_i + SE_i^2} \text{ (Eq. 2)}$$

179
$$SE_i = \frac{SD_i}{\sqrt{N_i}} \text{ (Eq. 3)}$$

180

181   where SD_i is the standard deviation of the daily values in grid cell i. The standard error measures how

182   far the sample mean could be from the true population mean.

183   Finally, when spatially averaging globally or regionally, under the assumption that the errors are

184   correlated across space, the overall uncertainty is calculated by averaging σ_i across the N_j grid cells

185   in spatial domain j weighted by the grid cell area fraction with respect to the total area (i.e., grid cell

186   / total area = w$_i$) with available retrievals:

187

188
$$\sigma_j = \sum_{i=1}^{N_j} w_i * \sigma_i \text{(Eq.4)}$$

189

190   **4. Results**

191

192   Our analysis is divided in two main parts. In the first one (Section 4.1) we assess the annual and

193   seasonal climatological DOD maps for nine distinct regions. In the second one (Section 4.2),

194   emphasis is given on the quantification of DOD averages along with their monthly and interannual

195   variability of the fractional contribution to the AOD, from a global to hemispherical level as well as

196   for specific regional domains.

197

198   *4.1 Annual and seasonal geographical distributions of DOD*

199

200   *4.1.1 North Africa, Tropical Atlantic Ocean and Mediterranean*

201

202   According to the long-term average map (Fig. 1), the maximum DODs (up to 1.2) are recorded in

203   the Bodélé depression, which is considered the most active individual dust source of the planet

204   (Washington et al., 2003; Koren et al., 2006; Ginoux et al., 2012). Over the area, the prevailing strong

205   winds are intensified further between the Tibesti mountains and the Ennedi ridge (Washington et al.,

206   2009) forming a low-level jet (Washington and Todd, 2005). This dominant wind pattern, affected

207   by the local topography (Washington et al., 2009), acts as the driving force mobilizing mineral

208   particles from arid and erodible soils of the region (Tegen et al., 2006). Under these favorable

209 conditions, dust aerosols are easily uplifted and accumulated in the atmosphere thus causing the very
210 high DODs (> 0.5) observed in the broader area (Chad, Niger). Throughout the year, the high DOD
211 levels are quite persistent exhibiting, however, a seasonal variation with more intense loads recorded
212 during DJF (Fig. S1-i) and MAM (Fig. S1-ii) following the annual cycle of source activation
213 (Washington et al., 2009). The second hotspot in N. Africa is situated between the northern parts of
214 Nigeria and the southern parts of Niger with annual DODs reaching up to 0.7 (Fig. 1) while on
215 seasonal basis vary from 0.4 (SON; Fig. S1-iv) to 0.8 (JJA; Fig. S1-iii). MIDAS DODs match well
216 with those presented by Rajot et al. (2008), who relied on ground-based sunphotometric
217 measurements of AOD obtained at the Banizoumbou AERONET site. Very high DODs are also
218 evident along the coasts of the Gulf of Guinea, which may be unrealistic considering that dust aerosols
219 are mainly transported there and are mixed with anthropogenic and biomass burning (Knippertz et
220 al., 2015). Along this area of high DODs, MERRA-2 also overestimates the dust fraction compared
221 to LIVAS (Gkikas et al., 2021) thus resulting in higher intensities according to the applied
222 methodology (Section 2). Moreover, the temporal availability of DODs in the region is very limited
223 (<10%; Fig. 8-c in Gkikas et al., 2021), the DOD uncertainty is large and AOD outliers, either realistic
224 or cloud contaminated, can yield exceptional high DODs in this complex environment where aerosol
225 and clouds are spatially correlated (Andrew Sayer, personal communication). This abrupt reduction
226 of DOD levels, from inland to the nearby maritime environment, reveals an artifact of the MIDAS
227 dataset mainly introduced by the raw MODIS AOD retrievals, which are obtained by retrieval
228 algorithms built on different assumptions/considerations depending on the underlying surface type.

229 Across the Sahara Desert, there is a distinct longitudinal contrast with more intense dust loads in
230 western North Africa than in eastern North Africa (Fig. 1). In the former sector, the DODs range
231 mainly from 0.3 to 0.6 while over the eastern parts of the Sahara the corresponding limits are bounded
232 between 0.1 and 0.3 without revealing significant intra-annual variation. During MAM (Fig. S1-ii),
233 along the southern Sahel, the activation of dust sources results in DODs which locally can exceed
234 0.8, while during boreal summer (Fig. S1-iii) a vast area of the western Sahara is under the impact of
235 heavy dust loadings (DOD > 0.5). According to Ginoux et al. (2012), in the former region, dust is
236 mainly produced by agricultural activities (cultivation, overgrazing) disturbing soils in which alluvial
237 sediments have been accumulated. Northwards, dust has natural origin and the accumulation of
238 mineral particles is favored by the development of the Saharan Heat Low (SHL) affecting also the
239 prevailing airflow (harmattan winds) as well as the West African Monsoon (WAM) (Schepanski et
240 al., 2017). Under these meteorological conditions, several dynamic processes, from mesoscale to
241 microscale, are taking place triggering dust emission (Knippertz and Todd, 2012) from highly active
242 sources (Schepanski et al., 2007).

243   Under the impact of the trade winds, Saharan dust can travel across the tropical Atlantic Ocean
244   reaching the Caribbean Sea, the southern United States and northeastern South America (Prospero,
245   1999; Prospero et al., 2014). The signal of this long-range transport is evident on the annual
246   climatological pattern (Fig. 1) with DODs up to 0.6 (off the western Saharan coasts) fading down to
247   0.1 at the maximum distance. Within the course of the year, the Saharan dust plume varies in terms
248   of intensity, range and latitudinal position, as it is depicted in Figure S1. During boreal summer (Fig.
249   S1-iii), the corridor of the transatlantic dust transport is bounded between 10° N and 20° N latitudes
250   whereas both the intensity (DODs up to 0.6) and the range are maximized. During boreal winter (Fig.
251   S1-i), the dust zone migrates southwards (between Equator and 10° N) while maximum (up to 0.6)
252   and considerable (0.1-0.2) DODs are observed over the Gulf of Guinea and mid-Atlantic (45° W),
253   respectively. Between the transition seasons (Fig. S1-ii, S1-iv), dust loads are stronger in MAM
254   (~0.45), mainly residing within 5° N and 20° N latitudes, in contrast to SON (~0.3) when are shifted
255   northwards (10° N and 25° N). According to the existing literature, several factors modulate the
256   westwards propagation of dust plumes, originating in the western Sahara and the Bodélé Depression,
257   over the tropical Atlantic. For instance, the south-north displacement of the Saharan plumes is driven
258   by the location of the Intertropical Convergence Zone (ITCZ) and the disturbances of the African
259   easterly jet (Knippertz and Todd, 2012; Doherty et al., 2012). Teleconnection patterns, such as the El
260   Niño–Southern Oscillation (ENSO; Prospero and Lamb, 2003), the North Atlantic Oscillation (NAO;
261   Ginoux et al., 2004) and the North African Dipole Index (NAFDI; Rodríguez et al., 2015) have been
262   also studied in order to interpret the decadal variations of dust concentrations over the Atlantic.
263   Likewise, the vegetation coverage across the Sahel as well as the wind speeds, determined by the
264   prevailing atmospheric circulation, over the Sahara play a key role on the amount of the emitted dust
265   particles.

266   Due to the vicinity of the largest deserts of the planet, the Mediterranean is affected by dust
267   outbreaks throughout the year (Gkikas et al., 2013; 2016; Marinou et al., 2017). Mineral particles
268   originating primarily from north African and secondarily from Middle Eastern deserts are transported
269   towards the Mediterranean mainly under the prevalence of cyclonic systems (Gkikas et al., 2015).
270   The intensity of dust loads decreases for increasing latitudes, forming a distinct south-north gradient
271   with DODs up to 0.20 between the gulfs of Gabes (Tunisia) and Sidra (Libya), according to the annual
272   pattern (Fig. 1). Among seasons (Fig. S1), DODs vary on the locations where the maximum levels
273   are recorded as well as on their magnitude, attributed to the position of the prevailing synoptic systems
274   (Gkikas et al., 2015). The central and eastern Mediterranean sectors are affected by dust loads mainly
275   in spring (DODs up to 0.3; Fig. S1-ii) and winter (DODs up to 0.12; Fig. S1-i). In summer (Fig. S1-
276   iii), dust activity is more pronounced in the western parts with optical depths up to 0.18 (Alboran
277   Sea), while thanks to the fine resolution product, "hotspots" of similar DODs can be identified in the

278   southern parts (Andalucia) of Spain. In SON (Fig. S1-iv), dust loads are found in the central
279   Mediterranean with DODs lower than 0.12 off the Tunisian and Libyan coasts.
280
281   *4.1.2 Middle East*
282
283   In the Middle East, there is a zone of moderate-to-high DODs (locally up to 0.8) extending from
284   Mesopotamia to the southern parts of the Saudi Arabia, where one of the largest sand deserts of the
285   world (Rub' al Khali) (Hamidi et al., 2013) is situated (Fig. 2). Based on Ginoux et al. (2012), the
286   origin of mineral particles between Tigris and Euphrates as well as across the Rub' al Khali Desert is
287   mainly natural while in the intermediate part (Ad-Dahna Desert) dust accumulation is attributed to
288   the mixing of anthropogenic and hydrological sources. Slightly higher maximum DODs (up to 0.7;
289   Fig. 2) are recorded in Oman and particularly between Dhofar and Al Wusta, in contrast to previous
290   studies (Pease et al., 1998) which have identified the Wahiba Sands area as a major dust source or the
291   coastal areas of Yemen (Ginoux et al., 2012). On a seasonal basis, the intensity of mineral loads
292   exhibits a strong variability with minimum DODs (up to 0.4) during DJF (Fig. S2-i) and SON (Fig.
293   S2-iv) and maximum (up to 1) during the dry period of the year (Figs S2-ii, S2-iii), being in agreement
294   with the results presented in Yu et al. (2013). More specifically, across the Arabian Peninsula, the
295   increase in DOD levels is getting evident in boreal spring and it is further intensified during summer
296   months. Dust storms emanating in Iraq and the eastern parts of Saudi Arabia favor dust transport
297   towards the Persian Gulf (Gianakopoulou and Toumi, 2012) account for the considerable high DOD
298   levels (>0.6) found there. Due to convergence of the northern-northernwesterly Shamal winds (Yu et
299   al., 2016) and the airflow from the subtropical anticyclone, in JJA, mineral particles are travelling at
300   even longer distances towards the northern Arabian Sea (Ramaswamy et al., 2017), as indicated by
301   the intense dust loads (DODs up to 0.5; Fig. S2-iii) contributing about half of the AOD (Jin et al.,
302   2018). Likewise, during boreal summer, short-range dust transport takes place off the coasts of Oman
303   and Yemen (Gulf of Aden). Among seas in the vicinity of the Arabian Peninsula, the most intense
304   dust loads are observed in the Red Sea, forming a clear latitudinal gradient on annual (Fig. 2) and
305   summer (Fig. S2-iii) geographical DOD patterns, as it has been noted also in Brindley et al. (2015)
306   and Banks et al. (2017). Due to its location, the southern sector of the Red Sea receives dust aerosols
307   either originating from the Republic of Sudan or from the Arabian Peninsula, depending on the zonal
308   airflow (Banks et al., 2017). Dusty air masses travelling westwards are uplifted when they are
309   crossing the mountain range in the southwestern Arabian Peninsula and for this reason dust loads
310   over the southern basin are suspended above 2 km (Banks et al., 2017). On the contrary, low-elevated
311   dust layers are recorded when winds blow from west, triggering dust emission from the Tokar Gap
312   (Sudanese coasts) and subsequently dust outflows into the southern Red Sea (Banks et al., 2017).

313

4.1.3   Central and southwest Asia

315

Northwards and eastwards of the Caspian Sea, various deserts are situated in the central segments of the Asian continent. Most part of Turkmenistan is occupied by the Karakum Desert while the Kyzylkum Desert is located in Uzbekistan. Other arid regions stretch between the Caspian and Aral Seas (Ustyurt plateau), in the eastern and southern flanks of the Aral Sea (Solonok Desert) and in the lowlands of western Kazakhstan and southeastern Russia (Ryn Desert) (Elguindi et al., 2016). Based on our seasonal spatial patterns (Fig. S3), the major dust activity is recorded in the Ustyurt Plateau (Li and Sokolik, 2018) and in the large lagoon embayment of Garabogazkol (Shen et al., 2016), a gulf of Turkmenistan dried into a salt-covered playa (Gills, 1996), with minimum (in DJF and SON) and maximum (in MAM and JJA) DODs equal to ~0.2 and ~0.4, respectively. In the rest of areas, the corresponding upper limits can reach up to 0.8-0.9, during boreal summer, in localized spots (Chimboy Lake, Sarygamysh Lake) across the Karakum and Kyzylkum Deserts. In the same season, moderate dust loadings (DOD up to 0.25) are encountered in the southern Caspian Sea (Elguindi et al., 2016) as the result of transported mineral particles mainly coming from the sandy deserts of Turkmenistan (Xi and Sokolik, 2015), under the impact of eastern/southeastern winds (Shen et al., 2016). Since the 1960s, the anthropogenic intervention (agricultural activities, over-irrigation) caused the retreat of the Aral Sea and the formation of the Aralkum Desert (Saiko and Zonn, 2000; Micklin, 2007) from which large amounts of aeolian dust are emitted and travel distances of hundreds of kilometers (Indoitu et al., 2015). According to the annual climatological map (Fig. 3), extremely high DODs (> 1) are found in the southeastern parts of the Aralkum Desert (Fig. 3) which are also persistent among the seasons (Fig. S3). Nevertheless, these are not trustworthy as it has been thoroughly discussed in Gkikas et al. (2021) (see Section 4.3.1).

In the Sistan basin, extending between Iran-Pakistan-Afghanistan, the long-term average JJA DODs can reach up to 1.1 (Figure S3-iii) in the Margo Desert (Afghanistan), due to the frequent occurrence of dust storms (Middleton, 1996), triggered by the northerly Levar winds, blowing from June to September (Alizadeh Choobari et al., 2014). These maximum DOD levels are substantially higher than the annual mean (0.8; Figure 3) as well as against the corresponding averages for the other seasons. Thanks to the high-resolution MIDAS DOD, we identify the borders of other active arid regions, surrounded by mountain ranges, such as the Rigestan (Afghanistan), the Balochistan (Pakistan), the Dasht-e-Kavir (Iran), the Dasht-e-Lut (Iran) and the Jazmurian drainage basin (Iran). In the aforementioned topographic lows, the magnitude of the dust loads is significantly lower than those observed in the Margo Desert and can be as large as 0.6 (Balochistan) during hot-dry months (Figure S3-iii). The presence of absorbing mineral particles, over the area and in the northernmost

349 part of the Arabian Sea, is also confirmed by the high AI values, especially in June-July, discussed
350 by Rashki et al. (2015), who relied on long-term records obtained by the OMI and TOMS spaceborne
351 sensors.
352
353 *4.1.4 Indian subcontinent*
354
355   In the Indian subcontinent, the maximum annual DODs (~0.5; Fig. 4) are observed along the Indus
356 river basin, in the western side of the Thar Desert whereas a branch of gradually decreasing DODs,
357 along the Indo-Gangetic plain towards eastwards directions, is also evident. Ginoux et al. (2012)
358 stated that much of dust activity in the Indus river basin is attributed to the suspension of soil particles
359 originating primarily from agricultural land use and to a lesser extent from the desiccation of
360 ephemeral water bodies. The strong presence of absorbing coarse particles over the area is further
361 supported by the coexistence of considerably high Aerosol Index (AI) values (Alam et al., 2011). As
362 indicated by the seasonal patterns (Fig. S4), the processes regulating the suspended dust loads are
363 highly variable during the year causing a remarkable temporal variability of DOD, which is low (<0.3)
364 in DJF and SON, moderate in MAM (<0.5) and maximum in JJA (<0.8). Similar seasonal variability
365 is evident in the Thar Desert, in agreement with the findings of Proestakis et al. (2018) and Dey and
366 Di Girolamo (2010), who used vertically-resolved (CALIOP) and multi-angle (MISR) satellite
367 retrievals, respectively. Nevertheless, our climatological DODs are higher with respect to the
368 CALIOP corresponding values and the MISR non-spherical AODs, particularly when dust activity
369 over the area is pronounced. During the pre-monsoon season, westerly to northwesterly winds are
370 blowing over the Thar Desert mobilizing dust particles which subsequently are advected towards the
371 Indo-Gangetic basin (Dey et al., 2004; Srivastava et al., 2011). According to our results, between the
372 Haryana state and the eastern parts of the plain, DODs fade down from ~0.6-0.7 to ~0.1-0.2, forming
373 a NW-SE gradient (Figs. S4-ii, S4-iii). Such high DODs are attributed to the eastwards propagation
374 of intense dust storms having a strong signature on the optical, microphysical and radiative properties
375 derived by AERONET stations operating in the region (Prasad et al., 2007a; Prasad et al., 2007b; Eck
376 et al., 2010).
377
378 *4.1.5 East Asia and North Pacific Ocean*
379
380   Northwards of the Tibetan Plateau is located the Tarim Basin (northwest China) in which one of
381 the largest natural dust source resides, the Taklamakan Desert. This elevated desert area (average
382 elevation 1.1 km) is surrounded by the Pamir Plateau (average elevation 5.5 km) in its west side, by
383 the Kunlun Shan range (average elevation 5.5 km) in its southern flanks and by the Tian Shan range

384 (average elevation 4.8 km) along its northern boundaries while only in its eastern margin the ground
385 elevation is low (Ge et al., 2014). DODs are maximized in spring (Fig. S5-ii) yielding values up to 1
386 along the foothills of the Tian Shan and Kunlun Shan ranges, attributed to the role of the topography
387 on winds strengthening (Ge et al., 2014). Similar values are recorded in JJA (Fig. S5-iii) but the
388 geographical distribution reveals that the highest DODs are less widespread in contrast to spring.
389 Throughout the year, the weaker dust loads are recorded during winter and autumn. Our results are
390 consistent with relevant studies that rely on active and passive satellite retrievals either of pure dust
391 load (Proestakis et al., 2018) or AOD (de Leeuw et al., 2018; Sogacheva et al., 2018).

392   A common feature in the seasonal DOD patterns is the reduction of dust loads' intensity towards
393 the interior parts of the Taklamakan Desert, as it has been also documented by Ge et al. (2014), who
394 utilized MISR retrievals. The high-resolution of the MIDAS DOD dataset provides in detail the
395 spatial information of these geographical patterns. During spring, similar high DODs to those found
396 over the Taklamakan Desert are recorded in the Qaidam Basin (northeast side of the Tibetan Plateau),
397 surrounded by the Atlun, Kunlun, Qilian mountain ranges, attributed to strong downslope winds
398 causing the erosion of soil particles (Rohrmann et al., 2013) and their entrainment into the
399 atmosphere. The intensity of dust loads over the Gobi Desert (north China – south Mongolia) hardly
400 exceeds 0.3 on an annual basis (Fig. 5) while it can reach up to 0.4 during spring (Fig. S5-iii). The
401 remarkable deviations in dust abundance between Taklamakan and Gobi during springtime are
402 interpreted by variations in soil characteristics. More specifically, Taklamakan is composed mainly
403 by fine sand particles in contrast to the rocky soils of the Gobi Desert (Sun et al., 2013). Due to these
404 differences in soil textures, dust particles from the former desert region can be emitted even with low
405 wind speeds while they are uplifted at higher elevations in the troposphere, as it has been shown with
406 MISR stereo observations (Yu et al., 2019) and CALIOP lidar profiles (Proestakis et al., 2018). The
407 injection of Taklamakan dust particles at higher altitudes increase their residence time inducing also
408 their entrainment into the upper-level westerly airflow, around at 4 a.m.s.l., both contributing to the
409 higher potential for long-range transport (Yu et al., 2019), in contrast to Gobi dust, towards the
410 continental E. Asia and the northern Pacific Ocean. Under the impact of cold fronts, propagating
411 eastwards (Eguchi et al., 2009) in spring, air masses carrying mineral particles, during the first two
412 days of dust transport, affect a wide area of China (Yu et al., 2019), from near sources to its eastern
413 parts, through the Hexi Corridor and the Loess Plateau (DODs ranging from 0.2 to 0.4; Fig. S5-iii).
414 Subsequently, the Asian dust plumes are suspended over the Yellow Sea, the Korean Peninsula and
415 further eastwards, in a latitudinal band bounded between the parallels 30°N and 45°, reaching the
416 west coasts of the United States (Yu et al., 2008). Across this "belt", where the Trans-pacific dust
417 transport is taking place, the springtime DODs decrease smoothly from 0.15 to 0.05 (Fig. S5-ii). In
418 summer (Fig. S5-iii), DODs up to 0.05 are observed between 40° N and 60° N indicating a northwards

419 displacement of the Asian dust layers (mainly originating from the Gobi Desert) due to the weakening
420 and northwards shift of the polar jet streams (Yu et al., 2019).
421
422 *4.1.6 North America*
423
424   Across N. America, the major dust activity is detected in southwest United States and in northwest
425 Mexico with annual and seasonal DODs hardly exceeding 0.15, as illustrated in Figures 6 and S6,
426 respectively. These weak dust load intensities are mainly recorded in the Sonoran and the Mojave
427 Deserts while lower values are found in the Chihuahuan Desert in which isolated spots (e.g. White
428 Sands Desert) become visible thanks to the high-resolution of the MIDAS DOD dataset. Low-to-
429 moderate DODs are evident in the Great Plains with local maxima (exceeding 0.2 in spring; Fig. S6-
430 ii) in the Great Salt Lake Desert and in the surrounding area as well as in the Baja Californian Desert
431 (Mexico; DODs up to 0.14), residing in the western side of the Gulf of California. Our annual spatial
432 distribution of DOD (Fig. 6) is highly consistent with those of frequency of observation (FoO) of
433 DOD (Ginoux et al., 2012; Baddock et al., 2016) and AI given by Prospero et al. (2002). Moreover,
434 the increase of dust loads' concentration in MAM (Fig. S6-ii), has been also documented by Hand et
435 al. (2016) and Tong et al. (2017), both relying on aerosol observations acquired at numerous stations
436 of the Interagency Monitoring of Protected Visual Environments (IMPROVE) network. During
437 springtime, dust emission over the broader area is associated with the transmit of Pacific cold fronts
438 inducing dust-entraining winds as the result of pressure gradient enhancement (Rivera Rivera et al.,
439 2009). The geomorphological soil characteristics are determinant for dust emission with the most
440 prominent natural sources being ephemeral and dry lakes (Baddock et al., 2016) while anthropogenic
441 dust aerosols are mainly emitted in the Great Plains and in the eastern side of the Gulf of California
442 (Ginoux et al., 2012).
443
444 *4.1.7 Australia*
445
446   Earlier studies based on unconstrained numerical simulations (Tanaka and Chiba, 2006; Wagener
447 et al., 2008) have shown that among the desert areas of the S. Hemisphere, the largest contribution of
448 dust particles arises from Australia. However, a more recent assessment (Kok et al., 2021b) in which
449 dust models have been constrained by observations revealed that the emitted dust amounts from S.
450 America are slightly higher than those of Australia. Due to the fairly bright landmasses and the
451 predominance of weak aerosol loadings, there is minimal contrast between surface and atmosphere
452 leading to systematic algorithm uncertainties, which can explain the slightly lower land DODs than
453 those recorded in the surrounding oceanic regions (Fig. 7 and S7). Nevertheless, in the sources as

454 well as in areas affected by dust plumes the atmospheric signal becomes evident. In particular, the
455 highest dust emissions are encountered in the Lake Eyre Basin (LEB; Prospero et al., 2002) composed
456 by ephemeral lakes, alluvial channels, gibber (stone-covered plains), aeolian sand deposits and
457 bedrocks (Bullard et al., 2008). Based on the annual climatological pattern (Fig. 7), DODs can locally
458 exceed 0.2 (in the southern parts) but in general vary between 0.06 and 0.12. From a seasonal
459 perspective (Fig. S7), the highest DODs (mainly up to 0.18 in the Warburton River estuary, few
460 exceedances above 0.4 are found in local spots) are recorded during austral summer (DJF; Fig. S7-i)
461 and spring (SON; Fig. S7-iv). Similar seasonal variation in ground-based sunphotometric
462 observations at nearby sites (Birdsville, Tinga Tingana), with slightly lower AODs, has been reported
463 by Mitchell et al. (2017). Southwards of the LEB, three spots of notable DODs (up to 0.2 in SON;
464 Fig. S7-iv) are identified in the Lakes Gairdner, Torrens and Frome while northeastwards (Lake
465 Yamma Yamma) and northwards (Simpson Desert) from the basin the suspended dust loads exhibit
466 optical depths as large as 0.12 during the driest months of the year. Similar maximum DODs are
467 recorded in the Northern Territory and in the western side of the Great Dividing Range (Queensland)
468 and in contrast to Ginoux et al. (2012) these levels appear in DJF instead of SON. In the southwestern
469 coastal parts of the Australian landmass as well as in Riverina (southeast), during austral spring (Fig.
470 S7-iv) very low DODs are evident associated with anthropogenic dust originating from agricultural
471 activities (Ginoux et al., 2012). Finally, during the same season, weak signals (DODs up to 0.05) of
472 dust transport are revealed over the Tasman and Timor Seas attributed to the eastward movement of
473 cyclonic frontal systems causing the entrainment of mineral particles in air masses that can travel at
474 long distances (Knight et al., 1995; Choobari et al., 2012).

476 *4.1.8 South Africa*

478   Dust activity in S. Africa is mainly related with short-range and short-lived plumes (Vickery et
479 al., 2013) that are suspended at low tropospheric altitudes (below 600 hPa) due to the predominance
480 of anticyclonic circulations inhibiting the vertical extension of dust layers (Piketh et al., 1999).
481 Mineral aerosol loadings are mainly originating from the ephemeral lake basins of the Etosha Pans
482 (Namibia) and Makgadikgadi Pans (Botswana) and the Namib Desert (Bryant et al., 2007; Vickery
483 et al., 2013). In the aforementioned source areas, the maximum annual (Figure 8) and seasonal (Figure
484 S8) DODs are equal to 0.1 and 0.16, respectively. Throughout the year, the increase of DODs in
485 Etosha and Makgadikgadi Pans is evident primarily in DJF (Figure S8-i) and secondarily in SON
486 (Figure S8-iv). Our results are consistent with those provided by Ginoux et al. (2012) and Bryant et
487 al. (2007) for the former region (including also the Kalahari Desert in which very weak dust loads are
488 recorded), contradictory for the latter one and opposite with the findings of Vickery et al. (2013) for

489   both sources. In these arid areas dust emission is linked with lakes' inundation, characterized by
490   strong intra-annual variability, playing an important role when different time periods are considered.
491   However, it must be also taken into account the moderate performance of the MERRA-2 dust portion
492   with respect to LIVAS in S. Africa as well as in most desert areas of the S. Hemisphere (Gkikas et
493   al., 2021). Along the Namibian coastline, the deviations of DOD between the high- and low-dust
494   seasons are small indicating that dust activity remains relatively constant within the course of the year
495   (Ginoux et al., 2012). Soil particles from salt pans and dry river beds of the Namib Desert are emitted
496   from aeolian processes related to bergwinds (katabatic winds) blowing in the escarpment, from the
497   Central Plateau down to the coasts (Eckardt and Kuring, 2005). Dust outflow towards the Southern
498   Atlantic Ocean, with a SE-NW orientation, it is shown between 18° S and 9° S during austral winter
499   (DODs up to 0.08; Fig. S8-iii), becoming more evident in SON (Fig. S8-iv), being in agreement with
500   the geographical distributions provided by Voss and Evan (2020). Such transport is favored by the
501   propagation of barotropic low-level easterly waves formed between continental high pressure systems
502   and the semi-permanent South Atlantic anticyclone (Tyson et al., 1996). Finally, weak signals of
503   DODs are recorded in the croplands north of Cape Town, with annual and DJF DODs not exceeding
504   0.1.
505
506   *4.1.9   South America*
507
508   In South America, the most intense dust loads are encountered in the Patagonia Desert where the
509   most active dust sources are situated in the river basins of the Rio Negro and Chubut provinces and
510   in its southern end. Among these areas, higher DODs (up to 0.16 in DJF; Figure S9-i) are found along
511   the Rio Negro attributed to anthropogenic dust originating from overgrazing, irrigation and oil
512   prospecting (McConnell, et al., 2007; Mazzonia and Vazquez, 2009). In southern latitudes, mineral
513   particles originate from glacier washout plains (Hernández et al., 2008). Under favorable
514   meteorological conditions, aeolian dust from Patagonia travels either towards the southern Atlantic
515   Ocean, contributing to iron concentrations and marine biological productivity in the surface waters
516   (Johnson et al., 2011), or towards the Antarctica peninsula (Gassó et al., 2010), as it has been found
517   in ice core samples (Basile et al., 1997). Both transport pathways are not visible in our climatological
518   patterns (Figures 9 and S9) since dust outbreaks are not so strong (Foth et al., 2019) while the
519   extended cloud coverage over the region results in large observational gaps of the spaceborne
520   retrievals (Gassó and Torres, 2019). Along the western side of Andes, dust emission arises from
521   natural sources located in the Sechura (Peru), Nazca (Peru) and Atacama (Chile) Deserts (Ginoux et
522   al., 2012). In the aforementioned regions, the annual DODs (Figure 9) can reach up to 0.1, 0.08 and
523   0.06, respectively, while the intra-annual variability is characterized weak (Figure S9). During MAM

524 (Figure S9-ii), DODs up to 0.16 appear in Guyana, Suriname and French Guiana as well as over their
525 offshore areas while similar intensities are evident in the northern parts of the Amazon rainforest
526 (around the Equator and bounded between 65°W and 60°W). The presence of coarse mineral particles
527 (Moran-Zuloaga, et al., 2018) over these distant areas from deserts, is attributed to the long-range
528 dust transport from North Africa across the Atlantic Ocean (Yu et al., 2015), under the impact of the
529 trade winds, taking place northwards of the convective precipitation zone formed around the ITCZ.
530 Finally, the latitudinal zone of weak DODs in the western parts of Brazil, fading down abruptly
531 eastwards of ~58° W, indicates an artifact of the MIDAS product that becomes more evident in SON
532 (Fig. S9-iv). This peculiar pattern is induced by the MERRA-2 dust fraction (results not shown here)
533 which is used for the derivation of MIDAS DOD from the MODIS AOD. An additional deficiency is
534 the relatively large DODs over an area where biomass burning particles, emitted at enormous amounts
535 by extended wildfires, clearly dominate over other aerosol species. Under these conditions, the non-
536 dust AODs are very high as well as their relevant uncertainties (Eqs. 5-7 in Gkikas et al. (2021)) while
537 the reliability of the MERRA-2 dust fraction downgrades there (see Fig. 2 in Gkikas et al. (2021)).
538
539 *4.2 DOD averages and variability at global, hemispherical and regional scales*
540
541   In this section, we discuss the average AOD and DOD along with their monthly and interannual
542 variability at global, hemispherical and regional scales. The left column of Figure 10 shows the
543 interannual timeseries of AOD (black curve) and DOD (red curve) averaged over the whole globe
544 (upper panel; GLB), the Northern Hemisphere (middle panel; NHE) and the Southern Hemisphere
545 (bottom panel; SHE). The right column of Figure 10 depicts the monthly seasonal cycle of AOD and
546 DOD along with the DOD-to-AOD ratio (blue curve) while the shaded areas correspond to the total
547 uncertainty (see Section 3.2 in Gkikas et al. (2021) and Section 3 in the current study).
548   The significant role of dust particles in the global aerosol budget becomes evident by visually
549 inspecting the AOD and DOD interannual timeseries (Fig. 10 i-a). The monthly contribution of
550 suspended dust to the total AOD varies from 14% to 39%, with minimum values mainly in DJF and
551 maximum values in MAM or JJA, depending on the year. Monthly DODs range from 0.016 ± 0.013
552 (Dec 2005) to 0.063 ± 0.028 (Mar 2012), whereas the long-term global annual average is equal to
553 0.032 ± 0.003 (Table 1). The global DOD mean, computed here from the fine resolution data, is
554 almost identical with those obtained by the coarse spatial resolution MERRA-2 and MIDAS DODs
555 and slightly higher than those calculated based on LIVAS-CALIOP (0.029) (see Table 1 in Gkikas et
556 al. (2021); it is noted the three datasets had been collocated based on the spatial resolution and the
557 temporal availability of the LIVAS dataset). Likewise, our global average and uncertainty computed
558 over the period 2004-2008 (0.033 ± 0.004) is close to the one obtained in Ridley et al. (2016) (0.030

559 ± 0.005), despite the different methods applied for the derivation of DOD and its uncertainty. Our
560 global DOD long-term average is very close to the CALIOP derived value (0.029) and about half of
561 the MODIS derived one (0.063) reported by Song et al. (2021).

562   Our continental (0.070 ± 0.005) and oceanic (0.019 ± 0.002) mean DODs (see Table 1) are
563 substantially lower than those obtained in Voss and Evan (2020) (land: 0.1; ocean: 0.03). This
564 difference may be attributed to the different averaging approaches, which can have an important
565 impact on the calculations as it has been shown in Levy et al. (2009) (see their Figure 5). Based on
566 our method, we are giving the same "weight" at each grid cell (regardless of the amount of available
567 data in that grid cell throughout the study period) when we are calculating the domain (from regional
568 to global) average. Therefore, we are avoiding an overestimation of the spatial average since MIDAS
569 data availability is larger over/nearby deserts (see Figure 8-c in Gkikas et al. (2021)) where the higher
570 DODs are observed. To be more specific, when we are calculating the global long-term DOD average
571 based on the second branch (i.e., "Straight", the standard approach for the calculation of the average
572 value by considering all the available values in space and time) in Levy et al. (2009), we obtain a
573 climatological value equal to 0.047. Such different approaches for the calculation of the long-term
574 DOD averages might interpret and the deviations found between this study and Song et al. (2021).
575 Finally, the computed global mean MIDAS DOD is somewhat higher than those simulated by most
576 AeroCom Phase I models (Huneeus et al., 2011), being about 40% higher than the median (0.023);
577 nevertheless, it must be taken into account that most models account for the diurnal variation of DOD
578 in contrast to the single-measurements taken during MODIS overpass.

579   As expected, the interannual GLB DOD timeseries is driven by the variability in the NHE DOD
580 (Figure 10 ii-a) since the most widespread and intense dust sources are located in the Northern
581 Hemisphere. This is justified by their high temporal co-variation while a positive NHE-GLB offset is
582 constantly observed, being lower during boreal winter and autumn (up to 0.035) and maximum during
583 the high dust seasons (0.058). The fraction of monthly NHE AOD attributed to dust particles ranges
584 from 20% to 48% and the R^2 value between monthly AOD and DOD is equal to 0.94, both indicating
585 a dominant dust contribution. Over the study period (2003-2017), the NHE DOD yields a
586 climatological mean equal to 0.056 ± 0.004 (Table 1) ranging from 0.024 ± 0.015 (Dec 2005) to 0.121
587 ± 0.050 (Mar 2012). In contrast, marine and biomass burning aerosols, rather than dust, regulate AOD
588 in the Southern Hemisphere (Figure 10 iii-a). SHE DODs are estimated to be low (0.008 ± 0.001),
589 with the maximum value (0.016 ± 0.016) recorded in February 2016. The contribution of dust aerosols
590 to the total aerosol load does not exceed 17% throughout the study period (Fig. 10 iii-a) and on
591 average it is equal to 8.2% ± 1.1%, which is in very good agreement with the findings by Kok et al.
592 (2021b).

593   A better view of the seasonal cycles of AOD, DOD and the DOD-to-AOD ratio can be obtained

594   by investigating their climatological patterns, representative for the period of interest (2003-2017).

595   On a global scale (Fig. 10 i-b), DODs peak between March and June (~0.045), and then decline until

596   November (0.018) before rising during boreal winter. Despite the monthly shifts between maximum

597   AOD and DOD averages, the seasonal cycles of the total aerosol and dust burdens are similar to a

598   large extent, whereas the contribution of mineral particles to the total extinction ranges from 16%

599   (November) to 33% (March-June). The MIDAS global DOD-to-AOD ratio (~23%) is close to the

600   values reported by Gelaro et al. (2017) and Kinne et al. (2006), ~22% and ~26%, respectively, but

601   higher than most of the model-derived estimations (12% - 28%) from the AeroCom Phase III (Gliss

602   et al., 2021). These discrepancies, excluding the aerosol parametrizations, may be partly due to the

603   different sampling between single-overpass satellite observations and reanalyses (Gelaro et al., 2017)

604   or models (Kinne et al., 2006) where the diurnal aerosol variability (Schepanski et al., 2009; Yu et

605   al., 2021) is included. In the NHE (Fig. 10 ii-b), the mean seasonal trend of DODs remains relatively

606   unchanged when compared with GLB; however, the hemispheric means (0.030-0.088) and the dust

607   fraction (24-41%) are higher. On the contrary, the weak signal of aeolian dust in SHE (Fig. 10 iii-b)

608   interprets the very low DODs (0.005 – 0.011) and their minor impact (6-12%) upon AOD magnitude.

609   The analysis presented above has also been conducted for each one of the 17 sub-regions

610   illustrated in Figure 7 in Gkikas et al. (2021), and the main findings are summarized in this paragraph.

611   Among the regional domains, a persistency of high DODs (>0.3), both at interannual and seasonal

612   scales, it is found only in BOD, which yields a long-term average value equal to 0.533 ± 0.009, being

613   almost double than WSA (0.302 ± 0.006) and TAK (0.246 ± 0.020) as illustrated in Table 1. However,

614   when focus is given to individual months, the maximum DODs over the study period (Fig. 11 vi-a)

615   and on their climatological levels are recorded in the Taklamakan Desert and can be as high as 0.868

616   (April 2007) and 0.600 (April), respectively. Comparable or even higher DODs than those computed

617   in BOD, are also evident for specific months in THA (Fig. 11 vii-a), GOG (Fig. 11 xii-a) and SSA

618   (Fig. 11 xv-a) as well as on the monthly timeseries (THA; Fig. 11 vii-b). Mineral particles'

619   contribution to the total AOD (i.e., blue curves in the seasonal cycle plots) is at least 50% over dust

620   sources or dust-abundant areas in N. Africa, Middle East and Asia and it is constantly higher than

621   70%, reaching up to 95%, in BOD (Fig. 11 i-b), WSA (Fig. 11 viii-b) and TAK (Fig. 11 vi-b). Over

622   downwind regions, such as EAS (Fig. 11 ix-b), GOG (Fig. 11 xii-b), MED (Fig. 11 xiii-b) and SSA

623   (Fig. 11 xv-b), the dust contribution can prevail over the non-dust portion (GOG, MED, SSA) while

624   in EAS does not exceed 30%, due to the predominance of anthropogenic aerosols. In the oceanic

625   areas of Tropical Atlantic and North Pacific, where large-scale dust transport is taking place, AOD

626   and DOD co-vary, indicating that the dust activity regulates the temporal variations of aerosols' load,

627   except during summer months in WNP (Fig. 11 xvi-a, xvi-b). Regarding the seasonal cycle of DOD,

628 the maximum values are recorded either during boreal spring (GOB, CAS, NME, SUS, TAK, EAS,
629 ENP, GOG, MED, WNP and SSA) or during boreal summer (THA, WSA, ETA, SME and WTA) or
630 are similar between the two high-dust seasons (BOD).

631 A final intercomparison of the MIDAS DODs against those derived by Ridley et al. (2016) and
632 Adebiyi et al. (2020), on a seasonal basis over the period 2004 - 2008, has been performed for 15
633 regions defined in Kok et al. (2021a) (see their Figure 2-b and Table 2). The obtained results are
634 illustrated in Figure 12. For the southern hemisphere regions (Figs. 12 –xiii, xiv, xv) as well as for
635 North America (Fig. 12-xii), MIDAS DODs are compared versus those from Adebiyi et al. (2020)
636 while for the remaining 11 domains (Figs. 12-i – xi) the results from Ridley et al. (2016) have been
637 utilized. As an overview, it is noted that the seasonal cycle among the three databases is commonly
638 reproduced, with a few exceptions (Mali-Niger, Kyzyl Kum, Southern Africa), whereas the DOD
639 uncertainties (represented by the error bars) are comparable. Regarding the magnitudes, MIDAS
640 DODs are mainly somewhat lower than those of Ridley et al. (2016) across the dust belt in contrast
641 to the outflow region of the Mid-Atlantic (Fig. 12-i). The obtained differences are mainly attributed
642 to the consideration of different models for accounting for the non-dust portion, the different
643 treatment of AODs (bias correction vs. quality filtering), the different versions of MODIS retrievals
644 (C006 vs C061), the consideration of multi-satellite observations instead of relying only on MODIS-
645 Aqua retrievals as well as to the different spatial scales (coarse vs. fine). In relative terms, the largest
646 deviations are found in the desert areas of the southern hemisphere where models struggle to represent
647 adequately the dust sources and the emitted amounts of mineral particles, thus affecting the dust
648 fraction ratio provided by MERRA-2.

649

650 **5. Summary and conclusions**

651

652 The current study presents a scientific exploitation of the MIDAS dataset (Gkikas et al., 2021),
653 which provides columnar mid-visible (550 nm) dust optical depth (DOD) at fine spatial resolution
654 (0.1° x 0.1°) and over a 15-year period (2003 – 2017). Taking advantage of the global coverage of
655 the MIDAS DOD product, we analyzed the contribution of dust aerosols to AOD at various spatial
656 and temporal scales. More specifically, we focused on 9 regions that account for the majority of the
657 global dust budget, encompassing sources and downwind areas with the main dust transport
658 pathways. Such regions comprise the deserts extending across the "dust belt", North America,
659 Australia, South Africa and South America as well as maritime areas (Tropical Atlantic Ocean,
660 Mediterranean, North Pacific Ocean) receiving constantly large amounts of mineral particles from
661 the nearby deserts. At a further step, the interannual and intra-annual timeseries of DODs along with

their contribution to the total aerosol load (AOD), were investigated at global, hemispherical and regional level.

According to our findings, the global long-term DOD average over the study period (2003-2017) is equal to 0.032 ± 0.003, yielding a strong contrast between the contributions from the northern (0.056 ± 0.004) and southern (0.008 ± 0.001) hemispheres. Our global estimations are almost identical with those given by Ridley et al. (2016) and the CALIOP-derived estimate of Song et al. (2021), in contrast to the MODIS-based average given from the latter study. Nevertheless, when the global averages are calculated separately over land (0.070 ± 0.005) and ocean (0.019 ± 0.002), our results differ substantially than those found in Voss and Evan (2020), who reported continental and maritime DODs equal to 0.100 and 0.030, respectively. Such large deviations are attributed to the different applied methodologies and averaging procedures followed. Moreover, we find very good agreement, in terms of DOD magnitude and uncertainty, of the MIDAS seasonal DODs versus those of Ridley et al. (2016) and Adebiyi et al. (2020) for 15 regions defined in Kok et al. (2021a). Considering that the long-term DOD averages can be utilized for constraining global dust in climate models, or can be used in several other applications, a detailed analysis is required for enlightening the factors resulting in disagreements among studies. Likewise, our computed global DOD average resides around the middle of the AeroCom (Huneeus et al., 2011) limits, being higher than the median (0.023) and mean (0.028). However, in the model-based calculations the diurnal variability is taken into account in contrast to the satellite-based estimations relying on single overpass measurements per day.

Regarding the dust contribution to the total aerosol optical depth, the DOD-to-AOD ratio from 32% at N. Hemisphere drops down to 8% in S. Hemisphere while at global scale is about one quarter (23%). The contradiction found between the two hemispheres, both for DOD and dust fraction, is interpreted by the most pronounced dust activity recorded in the Bodélé Depression of the northern Lake Chad Basin (DODs up to ~1.2), across the Sahel (DODs up to 0.8), in western parts of the Sahara Desert (DODs up to 0.6), in the eastern parts of the Arabian Peninsula (DODs up to ~1), along the Indus river basin (DODs up to 0.8) and in the Taklamakan Desert (DODs up to ~1). On the contrary, the weaker emission mechanisms triggering dust mobilization over the spatially limited sources of Patagonia, South Africa and interior arid areas of Australia do not favor the accumulation of mineral particles at large amounts (DODs up to 0.4 at local hotspots), even during high-dust seasons. Except for the Bodélé Depression, where the seasonal variability of the intense dust loads is relatively weak, in the other dust sources of the N. Hemisphere, DODs exhibit a strong seasonal cycle with maximum levels either during boreal spring or summer and minimum in boreal winter.

Over oceans, the main pathways of long-range dust transport are observed along the tropical Atlantic and the northern Pacific, revealing a remarkable variation, within the course of the year, in terms of intensity, latitudinal position and range. Saharan dust plumes, reaching the Caribbean Sea in

Deleted: The

Deleted: found with the latter study

summer under the impact of the trade winds, are more abundant with respect to Asian dust, arriving at the western coasts of the United States in spring under the impact of midlatitude cyclones. Due to the convergence of the Shamal winds, blowing over the Arabian Peninsula, and the wind flow from the subtropical anticyclone, dust aerosols originating in the Middle East can reach the western Indian coasts in summer, crossing the Arabian Sea. Dust loads in the southern parts of the Red Sea are maximized during boreal summer when Saharan or Middle East dust is transported, depending on the zonal airflow. The intensity of dust burden in the Mediterranean forms a south-north gradient, whereas a seasonal longitudinal shift of the maximum DODs, off the northern African coasts, is evident attributed to the prevailing synoptic circulation.

Despite the strong capabilities of the MIDAS dataset, we have also been identified some limitations, thoroughly discussed here and in Gkikas et al. (2021), attributed either to inherent weaknesses of the raw MODIS AOD retrievals or to deficiencies of MDF, resulting in not too realistic patterns in specific regions of the planet. Thanks to this detailed analysis, potential users are aware of any issue that may rise when utilizing the MIDAS DOD product. Moreover, it is among our priorities to minimize the impacts of these drawbacks in future versions of the MIDAS dataset.

As already mentioned, a variety of research studies can rely on the MIDAS dataset. MIDAS has been already used for the investigation of DOD trends (Logothetis et al., 2021) whereas in a follow-up study the mechanisms contributing to the temporal variations of dust burden will be investigated. Likewise, the MIDAS DOD product has been utilized in radiative transfer studies (Fountoulakis et al, 2021; Masoom et al., 2021) focusing on the impacts on solar energy production. Moreover, taking advantage of the fine spatial resolution of the MIDAS dataset and of its extended temporal availability, the dataset can be used for the identification of dust sources worldwide, similarly to the analysis done in Ginoux et al. (2012). Finally, we have provided a simple, yet flexible method (independent from other datasets) to calculate consistent uncertainties across spatiotemporal scales, which will ease the use of the MIDAS dataset in data assimilation applications.

Acknowledgments

Antonis Gkikas acknowledges support by the Hellenic Foundation for Research and Innovation (H.F.R.I.) under the "2nd Call for H.F.R.I. Research Projects to support Post-Doctoral Researchers" (Project Acronym: ATLANTAS, Project Number: 544). Vassilis Amiridis acknowledges support from the European Research Council (grant no. 725698; D-TECT). Eleni Marinou was funded by a DLR VO-Ryoung investigator group and the Deutscher Akademischer Austauschdienst (grant no. 57370121). Jasper F. Kok acknowledges support from National Science Foundation (NSF) grant 1552519. Carlos Pérez García-Pando acknowledges support from the European Research Council (grant no. 773051; FRAGMENT), the AXA Research Fund, and the Spanish Ministry of Science,

748 Innovation and Universities (grant nos. RYC-2015-18690 and CGL2017- 88911-R). The authors
749 acknowledge support from the DustClim project as part of ERA4CS, an ERA-NET project initiated
750 by JPI Climate and funded by FORMAS (SE), DLR (DE), BMWFW (AT), IFD (DK), MINECO
751 (ES), and ANR (FR), with cofunding by the European Union (grant no. 690462). PRACE (Partnership
752 for Advanced Computing in Europe) and RES (Red Española de Supercomputación) are
753 acknowledged for awarding access to the MareNostrum Supercomputer in the Barcelona
754 Supercomputing Center. We acknowledge support of this work by the PANhellenic infrastructure for
755 Atmospheric Composition and climatE chAnge (PANACEA) project (grant no. MIS 5021516),
756 which is implemented under the Horizon 2020 Action of "Reinforcement of the Research and
757 Innovation Infrastructure", funded by the Operational Programme Competitiveness,
758 Entrepreneurship, and Innovation (NSRF 2014–2020) and cofinanced by Greece and the European
759 Union (under the European Regional Development Fund). NOA members acknowledge support from
760 the Stavros Niarchos Foundation (SNF). The authors acknowledge support by the COST Action
761 "InDust" (grant no. CA16202), supported by COST (European Cooperation in Science and
762 Technology). The authors would like to thank Andrew Mark Sayer for his valuable and constructive
763 comments. The authors would like also to thank Thanasis Georgiou for developing the ftp server on
764 which the MIDAS data set is stored.

765

766 **Data availability**

767

768 The MIDAS dataset has been developed in the framework of the DUST-GLASS project (grant no.
769 749461; European Union's Horizon 2020 Research and Innovation programme under the Marie
770 Skłodowska-Curie Actions) and it is available at: https://doi.org/10.5281/zenodo.4244106.

771

772 **References**
773 Adebiyi, A. A., Kok, J. F., Wang, Y., Ito, A., Ridley, D. A., Nabat, P., and Zhao, C.: Dust Constraints
774 from joint Observational-Modelling-experiMental analysis (DustCOMM): comparison with
775 measurements and model simulations, Atmos. Chem. Phys., 20, 829–863,
776 https://doi.org/10.5194/acp-20-829-2020, 2020.

777 Alam, K., Qureshi, S., & Blaschke, T.: Monitoring spatio-temporal aerosol patterns over Pakistan
778 based on MODIS, TOMS and MISR satellite data and a HYSPLIT model. Atmospheric Environment,
779 45, 4641–4651, 2011.

780 Alizadeh-Choobari, O., Zawar-Reza, P., Sturman, A.: The "wind of 120 days" and dust storm activity
781 over the Sistan Basin, *Atmos. Res., 143*, 328–341, 2014.

782

783 Amiridis, V., Wandinger, U., Marinou, E., Giannakaki, E., Tsekeri, A., Basart, S., Kazadzis, S.,
784 Gkikas, A., Taylor, M., Baldasano, J., and Ansmann, A.: Optimizing CALIPSO Saharan dust
785 retrievals, Atmos. Chem. Phys., 13, 12089–12106, https://doi.org/10.5194/acp-13-12089-2013, 2013.
786

787 Amiridis, V., Marinou, E., Tsekeri, A., Wandinger, U., Schwarz, A., Giannakaki, E., Mamouri, R.,
788 Kokkalis, P., Binietoglou, I., Solomos, S., Herekakis, T., Kazadzis, S., Gerasopoulos, E., Proestakis,
789 E., Kottas, M., Balis, D., Papayannis, A., Kontoes, C., Kourtidis, K., Papagiannopoulos, N., Mona,
790 L., Pappalardo, G., Le Rille, O., and Ansmann, A.: LIVAS: a 3-D multi-wavelength aerosol/cloud
791 database based on CALIPSO and EARLINET, Atmos. Chem. Phys., 15, 7127-7153,
792 https://doi.org/10.5194/acp-15-7127-2015, 2015.
793

794 Baddock, M. C., Ginoux, P., Bullard, J. E., and Gill, T. E.: Do MODIS-defined dust sources have a
795 geomorphological signature?, Geophys. Res. Lett., 43, GL067327, doi:10.1002/2015GL067327,
796 2016.
797

798 Banks, J. R., Brindley, H. E., Stenchikov, G., and Schepanski, K.: Satellite retrievals of dust aerosol
799 over the Red Sea and the Persian Gulf (2005–2015), Atmos. Chem. Phys., 17, 3987-4003,
800 https://doi.org/10.5194/acp-17-3987-2017, 2017.
801

802 Basile, I., Grousset, F. E., Revel, M., Petit, J.-R., Biscaye, P. E., and Barkov, N. I.: Patagonian origin
803 of glacial dust deposited in East Antarctica (Vostok and Dome C) during glacial stages 2, 4 and 6,
804 Earth Planet. Sc. Lett., 146, 573–589, 1997.
805

806 Brindley, H., Osipov, S., Bantges, R., Smirnov, A., Banks, J., Levy, R., Jish Prakash, P., and
807 Stenchikov, G.: An assessment of the quality of aerosol retrievals over the Red Sea and evaluation of
808 the climatological cloud-free dust direct radiative effect in the region, J. Geophys. Res.-Atmos., 120,
809 10862–10878, doi:10.1002/2015JD023282, 2015.
810

811 Bryant, R. G., Bigg, G. R., Mahowald, N. M., Eckardt, F. D., and Ross S. G.: Dust emission response
812 to climate in southern Africa, J. Geophys, Res, 112, D09207, doi:10.1029/2005JD007025, 2007.
813

814 Bullard, J. E., and Austin, M. J.: Dust generation on a proglacial floodplain, West Greenland. Aeolian
815 Res. 3, 43–54. doi: 10.1016/j.aeolia.2011.01.002, 2011, 2017.
816

817   Bullard, J. E., Baddock, M., Bradwell, T., Crusius, J., Darlington, E., Gaiero, D., Gassó, S.,
818   Gisladottir, G., Hodgkins, R., McCulloch, R., McKenna-Neuman, C., Mockford, T., Stewart, H., and,
819   Thorsteinsson, T.: High-latitude dust in the Earth system, Rev. Geophys., 54, 447–485,
820   https://doi.org/10.1002/2016RG000518, 2016.

821

822   Bullard, J., Baddock, M., McTainsh, G. H., and Leys, J. F.: Subbasin scale dust source
823   geomorphology detected using MODIS, Geophys. Res. Lett., 35, L15404,
824   doi:10.1029/2008GL033928, 2008.

825   Chin, M., Ginoux, P., Kinne, S., Torres, O., Holben, B. N., Duncan, D. N., Martin, R. V., Logan, J.
826   A., Higurashi, H., and Nakajima, T.: Tropospheric aerosol optical thickness from the GOCART
827   model and comparisons with satellite and Sun photometer measurements, J. Atmos. Sci., 59, 451–
828   483, https://doi.org/10.1175/1520-0469(2002)059<0461:TAOTFT>2.0.CO;2, 2002.

829

830   de Leeuw, G., Sogacheva, L., Rodriguez, E., Kourtidis, K., Georgoulias, A. K., Alexandri, G.,
831   Amiridis, V., Proestakis, E., Marinou, E., Xue, Y., and van der A, R.: Two decades of satellite
832   observations of AOD over mainland China using ATSR-2, AATSR and MODIS/Terra: data set
833   evaluation and large-scale patterns, Atmos. Chem. Phys., 18, 1573-1592, https://doi.org/10.5194/acp-
834   18-1573-2018, 2018.

835

836   Dey, S. and Di Girolamo, L.: A climatology of aerosol optical and microphysical properties over the
837   Indian subcontinent from 9 years (2000–2008) of Multiangle Imaging Spectroradiometer (MISR)
838   data, J. Geophys. Res.-Atmos., 115, D15204, https://doi.org/10.1029/2009JD013395, 2010.

839

840   Dey, S., Tripathi, S. N., Singh, R. P., and Holben, B. N.: Influence of dust storms on the aerosol
841   optical properties over the Indo-Gangetic basin, J. Geophys. Res.-Atmos., 109, 1–10,
842   doi:10.1029/2004jd004924, 2004.

843

844   Di Tomaso, E., Schutgens, N. A. J., Jorba, O., and Pérez García-Pando, C.: Assimilation of MODIS
845   Dark Target and Deep Blue observations in the dust aerosol component of NMMB-MONARCH
846   version 1.0, Geosci. Model Dev., 10, 1107-1129, https://doi.org/10.5194/gmd-10-1107-2017, 2017.

847

848   Doherty, O. M., Riemer, N., and Hameed, S.: Control of Saharan mineral dust transport to Barbados
849   in winter by the Intertropical Convergence Zone over West Africa: Winter dust in Barbados and the
850   ITCZ, J. Geophys. Res.-Atmos., 117, D19117, doi:10.1029/2012JD017767, 2012.

851

Du, Y., Xu, X., Chu, M., Guo, Y., and Wang, J.: Air particulate matter and cardiovascular disease: the epidemiological, biomedical and clinical evidence, J. Thorac. Dis., 8, E8, https://doi.org/10.3978/j.issn.2072-1439.2015.11.37, 2016.

Eck, T. F., Holben, B. N., Sinyuk, A., Pinker, R. T., Goloub, P., Chen, H., Chatenet, B., Li, Z., Singh, R. P., and Tripathi, S. N.: Climatological aspects of the optical properties of fine/coarse mode aerosol mixtures, J. Geophys. Res.-Atmos., 115, 19205, https://doi.org/10.1029/2010JD014002, 2010.

Eckardt, F.D. Kuring, N.: SeaWiFS identifies dust sources in the Namib Desert. International Journal of Remote Sensing, 26:4159–4167, 2005.

Eguchi, K., Uno, I., Yumimoto, K., Takemura, T., Shimizu, A., Sugimoto, N., and Liu, Z.: Trans-pacific dust transport: integrated analysis of NASA/CALIPSO and a global aerosol transport model, Atmos. Chem. Phys., 9, 3137-3145, https://doi.org/10.5194/acp-9-3137-2009, 2009.

Elguindi, N., Solmon, F., Turuncoglu, U.: Quantifying some of the impacts of dust and other aerosol on the Caspian Sea region using a regional climate model. Clim. Dyn., 46, 41–55, 2016.

Fiedler, S., Schepanski, K., Heinold, B., Knippertz, P., and Tegen, I.: Climatology of nocturnal low-level jets over North Africa and implications for modeling mineral dust emission, J. Geophys. Res.-Atmos., 118, 6100–6121, 2013.

Flaounas, E., Kotroni, V., Lagouvardos, K., Kazadzis, S., Gkikas, A., and Hatzianastassiou, N.: Cyclone contribution to dust transport over the Mediterranean region, Atmos. Sci. Lett., 16, 473–478, doi:10.1002/asl.584, 2015.

Foth, A., Kanitz, T., Engelmann, R., Baars, H., Radenz, M., Seifert, P., Barja, B., Fromm, M., Kalesse, H., and Ansmann, A.: Vertical aerosol distribution in the southern hemispheric midlatitudes as observed with lidar in Punta Arenas, Chile (53.2° S and 70.9° W), during ALPACA, Atmos. Chem. Phys., 19, 6217–6233, https://doi.org/10.5194/acp-19-6217-2019, 2019.

Fountoulakis, Ilias, Panagiotis Kosmopoulos, Kyriakoula Papachristopoulou, Ioannis-Panagiotis Raptis, Rodanthi-Elisavet Mamouri, Argyro Nisantzi, Antonis Gkikas, Jonas Witthuhn, Sebastian Bley, Anna Moustaka, Johannes Buehl, Patric Seifert, Diofantos G. Hadjimitsis, Charalampos Kontoes, and Stelios Kazadzis. 2021. "Effects of Aerosols and Clouds on the Levels of Surface Solar

Radiation and Solar Energy in Cyprus" Remote Sensing 13, no. 12: 2319. https://doi.org/10.3390/rs13122319

Gassó, S., Stein, A., Marino, F., Castellano, E., Udisti, R., and Ceratto, J.: A combined observational and modeling approach to study modern dust transport from the Patagonia desert to East Antarctica, Atmos. Chem. Phys., 10, 8287-8303, https://doi.org/10.5194/acp-10-8287-2010, 2010.

Gassó, S., & Torres, O.: Temporal characterization of dust activity in the Central Patagonia desert (years 1964–2017), Journal of Geophysical Research: Atmospheres, 124, 3417– 3434. https://doi.org/10.1029/2018JD030209, 2019.

Ge, J. M., Huang, J. P., Xu, C. P., Qi, Y. L., and Liu, H. Y.: Characteristics of Taklimakan dust emission and distribution: a satellite and reanalysis field perspective, J. Geophys. Res.-Atmos., 119, 11772–11783, https://doi.org/10.1002/2014JD022280, 2014.

Gelaro, R, McCarty, W., Suárez, M. J., Todling, R., Molod, A., Takacs, L., Randles, C. A., Darmenov, A., Bosilovich, M. G., Reichle, R., Wargan, K., Coy, L., Cullather, R., Draper, C., Akella, S., Buchard, V., Conaty, A., da Silva, A. M., Gu, W., Kim, G., Koster, R., Lucchesi, R., Merkova, D., Nielsen, J. E., Partyka, G., Pawson, S., Putman, W., Rienecker, M., Schubert, S. D., Sienkiewicz, M., and Zhao, B.: The Modern-Era Retrospective Analysis for Research and Applications, Version 2 (MERRA-2), J. Climate, 30, 5419–5454, https://doi.org/10.1175/JCLI-D-16-0758.1, 2017.

Gill, T. E.: Eolian sediments generated by anthropogenic disturbance of playas: human impacts on the geomorphic system and geomorphic impacts on the human system, Geomorphology, 17, 207–228, 1996.

Ginoux, P., Prospero, J. M., Torres, O., and Chin, M.: Longterm simulation of global dust distribution with the GOCART model: correlation with North Atlantic Oscillation, Environ. Modell. Softw., 19, 113–128, https://doi.org/10.1016/S1364- 8152(03)00114-2, 2004.

Ginoux, P., Prospero, J. M., Gill, T. E., Hsu, N. C., and Zhao, M.: Global-scale attribution of anthropogenic and natural dust sources and their emission rates based on MODIS Deep Blue aerosol products, Rev. Geophys., 50, RG3005, https://doi.org/10.1029/2012RG000388, 2012.

Deleted: ¶

Gkikas, A., Hatzianastassiou, N., Mihalopoulos, N., Katsoulis, V., Kazadzis, S., Pey, J., Querol, X., and Torres, O.: The regime of intense desert dust episodes in the Mediterranean based on contemporary satellite observations and ground measurements, Atmos. Chem. Phys., 13, 12135-12154, https://doi.org/10.5194/acp-13-12135-2013, 2013.

Gkikas, A., Houssos, E. E., Lolis, C. J., Bartzokas, A., Mihalopoulos, N., and Hatzianastassiou, N.: Atmospheric circulation evolution related to desert-dust episodes over the Mediterranean, Q. J. Roy. Meteor. Soc., 141, 1634–1645, doi:10.1002/qj.2466, 2015.

Gkikas, A., Basart, S., Hatzianastassiou, N., Marinou, E., Amiridis, V., Kazadzis, S., Pey, J., Querol, X., Jorba, O., Gassó, S., and Baldasano, J. M.: Mediterranean intense desert dust outbreaks and their vertical structure based on remote sensing data, Atmos. Chem. Phys., 16, 8609-8642, https://doi.org/10.5194/acp-16-8609-2016, 2016.

Gkikas, A., Obiso, V., Pérez García-Pando, C., Jorba, O., Hatzianastassiou, N., Vendrell, L., Basart, S., Solomos, S., Gassó, S., and Baldasano, J. M.: Direct radiative effects during intense Mediterranean desert dust outbreaks, Atmos. Chem. Phys., 18, 8757-8787, https://doi.org/10.5194/acp-18-8757-2018, 2018.

Gkikas, A., Giannaros, T.M., Kotroni, V., Lagouvardos, K.: Assessing the radiative impacts of an extreme desert dust outbreak and the potential improvements on short-term weather forecasts: The case of February 2015, Atmos. Res., 226, 152-170, https://doi.org/10.1016/j.atmosres.2019.04.020, 2019.

Gkikas, A., Proestakis, E., Amiridis, V., Kazadzis, S., Di Tomaso, E., Tsekeri, A., Marinou, E., Hatzianastassiou, N., and Pérez García-Pando, C.: ModIs Dust AeroSol (MIDAS): a global fine-resolution dust optical depth data set, Atmos. Meas. Tech., 14, 309–334, https://doi.org/10.5194/amt-14-309-2021, 2021.

Gliß, J., Mortier, A., Schulz, M., Andrews, E., Balkanski, Y., Bauer, S. E., Benedictow, A. M. K., Bian, H., Checa-Garcia, R., Chin, M., Ginoux, P., Griesfeller, J. J., Heckel, A., Kipling, Z., Kirkevåg, A., Kokkola, H., Laj, P., Le Sager, P., Lund, M. T., Lund Myhre, C., Matsui, H., Myhre, G., Neubauer, D., van Noije, T., North, P., Olivié, D. J. L., Rémy, S., Sogacheva, L., Takemura, T., Tsigaridis, K., and Tsyro, S. G.: AeroCom phase III multi-model evaluation of the aerosol life cycle and optical

properties using ground- and space-based remote sensing as well as surface in situ observations, Atmos. Chem. Phys., 21, 87–128, https://doi.org/10.5194/acp-21-87-2021, 2021.

Hamidi, M., Kavianpour, M. R., and Shao, Y.: Synoptic analysis of dust storms in the Middle East, Asia-Pac. J. Atmos. Sci., 49, 279–286, 2013.

Hand, J. L., Gill, T. E., and Schichtel, B. A.: Spatial and seasonal variability in fine mineral dust and coarse aerosol mass at re-mote sites across the United States, J. Geophys. Res.-Atmos.,122, 3080–3097, https://doi.org/10.1002/2016jd026290, 2017.

Haywood, J. and Boucher, O.: Estimates of the direct and indirect radiative forcing due to tropospheric aerosols: A review, Rev. Geophys., 38, 513–543, https://doi.org/10.1029/1999RG000078, 2000.

Huang, J., Lin, B., Minnis, P., Wang, T., Wang, X., Hu, Y., Yi, Y., and Ayers, J. K.: Satellite-based assessment of possible dust aerosols semi-direct effect on cloud water path over East Asia, Geophys. Res. Lett., 33, L19802,https://doi.org/10.1029/2006GL026561, 2006.

Huneeus, N., Schulz, M., Balkanski, Y., Griesfeller, J., Prospero, J., Kinne, S., Bauer, S., Boucher, O., Chin, M., Dentener, F., Diehl, T., Easter, R., Fillmore, D., Ghan, S., Ginoux, P., Grini, A., Horowitz, L., Koch, D., Krol, M. C., Landing, W., Liu, X., Mahowald, N., Miller, R., Morcrette, J.-J., Myhre, G., Penner, J., Perlwitz, J., Stier, P., Takemura, T., and Zender, C. S.: Global dust model intercomparison in AeroCom phase I, Atmos. Chem. Phys., 11, 7781-7816, https://doi.org/10.5194/acp-11-7781-2011, 2011.

Husar, R. B., Tratt, D. M., Schichtel, D. M., Falke, S. R., Li, F., Jaffe, D., Gassó, S., Gill, T., Laulainen, N. S., Lu, F., Reheis, M. C., Chun, Y., Westphal, D., Holben, B. N., Gueymard, C., McK-endry, I., Kuring, N., Feldman, G. C., McClain, C., Frouin, R. J., Merrill, J., DuBois, D., Vignola, F., Murayama, T., Nickovic, S., Wilson, W. E., Sassen, K., Sugimoto, N., and Malm, W. C.: Asian dust events of April 1998, J. Geophys. Res., 106, 18317–18330, https://doi.org/10.1029/2000JD900788, 2001.

Ignatov, A. and Stowe, L.: Physical Basis, Premises, and SelfConsistency Checks of Aerosol Retrievals from TRMM VIRS, J. Appl. Meteor., 39, 2259–2277, https://doi.org/10.1175/1520-0450(2001)040<2259:PBPASC>2.0.CO;2, 2000.

991

992 Indoitu, R., Kozhoridze, G., Batyrbaeva, M., Vitkovskaya, I., Orlovsky, N., Blumberg, D., Orlovsky,
993 L.: Dust emission and environmental changes in the dried bottom of the Aral Sea. Aeolian. Res. 17,
994 101–115, 2015, https://doi.org/10.1016/j.aeolia.2015.02. 004.

995

996 Jickells, T. D., An, Z. S., Andersen, K. K., Baker, A. R., Bergametti, G., Brooks, N., Cao, J. J., Boyd,
997 P. W., Duce, R. A., Hunter, K. A., Kawahata, H., Kubilay, N., laRoche, J., Liss, P. S., Mahowald, N.,
998 Prospero, J. M., Ridgwell, A. J., Tegen, I., and Torres, R.: Global iron connections between desert
999 dust, ocean biogeochemistry, and climate, Science, 308, 67–71, 2005.

1000

1001 Jickells, T., Boyd, P., and Hunter, K.: Biogeochemical impacts of dust on the global carbon cycle, in:
1002 Mineral Dust, edited by: Knippertz, P. and Stuut, J.-B. W., Springer, the Netherlands, 359– 384, 2014.

1003

1004 Jin, Q., Wei, J., Pu, B., Yang, Z.-L., and Parajuli, S. P.: High summertime aerosol loadings over the
1005 Arabian Sea and their transport pathways. Journal of Geophysical Research:
1006 Atmospheres,123,10,568–10,590, https://doi.org/10.1029/2018JD028588, 2018.

1007

1008 Johnson, M. S., Meskhidze, N., Kiliyanpilakkil, V. P., and Gassó, S.: Understanding the transport of
1009 Patagonian dust and its influence on marine biological activity in the South Atlantic Ocean, Atmos.
1010 Chem. Phys., 11, 2487-2502, https://doi.org/10.5194/acp-11-2487-2011, 2011.

1011

1012 Kanakidou, M., Mihalopoulos, N., Kindap, T., Im, U., Vrekoussis, M., Gerasopoulos, E., Dermitzaki,
1013 E., Unal, A., Kocak, M., Markakis, K., Melas, D., Kouvarakis, G., Youssef, A. F., Richter, A.,
1014 Hatzianastassiou, N., Hilboll, A., Ebojie, F., Wittrock, F., von Savigny, C., Burrows, J. P.,
1015 Ladstaetter-Weissenmayer, A., and Moubasher, H.: Megacities as hot spots of air pollution in the
1016 East Mediterranean, Atmos. Environ., 45, 1223–1235,
1017 https://doi.org/10.1016/j.atmosenv.2010.11.048, 2011.

1018

1019 Kanatani, K.T., Ito, I., Al-Delaimy, W.K., Adachi, Y., Mathews, W.C., Ramsdell, J.W.: Toyama
1020 Asian Desert Dust and Asthma Study Group Members. Desert dust exposure is associated with
1021 increased risk of asthma hospitalization in children, Am. J. Respir. Crit. Care Med. 182 (12),
1022 1475e1481. https://doi.org/10. 1164/rccm.201002-0296OC, 2010.

1023

1024 Kinne, S., Schulz, M., Textor, C., Guibert, S., Balkanski, Y., Bauer, S. E., Berntsen, T., Berglen, T.
1025 F., Boucher, O., Chin, M., Collins, W., Dentener, F., Diehl, T., Easter, R., Feichter, J., Fillmore, D.,

1026 Ghan, S., Ginoux, P., Gong, S., Grini, A., Hendricks, J., Herzog, M., Horowitz, L., Isaksen, I., Iversen,
1027 T., Kirkevåg, A., Kloster, S., Koch, D., Kristjansson, J. E., Krol, M., Lauer, A., Lamarque, J. F.,
1028 Lesins, G., Liu, X., Lohmann, U., Montanaro, V., Myhre, G., Penner, J., Pitari, G., Reddy, S., Seland,
1029 O., Stier, P., Takemura, T., and Tie, X.: An AeroCom initial assessment – optical properties in aerosol
1030 component modules of global models, Atmos. Chem. Phys., 6, 1815-1834,
1031 https://doi.org/10.5194/acp-6-1815-2006, 2006.

1033 Klose, M., Shao, Y., Karremann, M. K., and Fink, A.: Sahel dust zone and synoptic background,
1034 Geophys. Res. Lett., 37, L09802, https://doi.org/10.1029/2010GL042816, 2010.

1036 Knight, A. W., McTainsh, G. H., & Simpson, R. W.: Sediment loads in an Australian dust storm—
1037 Implications for present and past dust processes. Catena, 24(3), 195–213,
1038 https://doi.org/10.1016/0341-8162(95)00026-O, 1995.

1040 Knippertz, P., Deutscher, C., Kandler, K., Müller, T., Schulz, O., and Schütz, L.: Dust mobilization
1041 due to density currents in the Atlas region: Observations from the Saharan Mineral Dust Experiment
1042 2006 field campaign, J. Geophys. Res.-Atmos., 112, 1–14, https://doi.org/10.1029/2007JD008774,
1043 2007.

1045 Knippertz, P., Evans, M., Field, P. R., Fink, A. H., Liousse, C., and Marsham, J. H.: The possible role
1046 of local air pollution in climate change in West Africa, Nat. Clim. Chang., 5, 815–822,
1047 https://doi.org/10.1038/NCLIMATE2727, 2015.

1049 Knippertz, P. and Todd, M. C.: Mineral Dust Aerosols over the Sahara: Meteorological Controls on
1050 Emission and Transport and Implications for Modeling, Rev. Geophys., 50, RG1007,
1051 https://doi.org/10.1029/2011RG000362, 2012.

1053 Koch, J. and Renno, N. O.: The role of convective plumes and vortices on the global aerosol budget,
1054 Geophys. Res. Lett., 32, L18806, doi:10.1029/2005GL023420, 2005.

1056 Kok, J. F., Adebiyi, A. A., Albani, S., Balkanski, Y., Checa-Garcia, R., Chin, M., Colarco, P. R.,
1057 Hamilton, D. S., Huang, Y., Ito, A., Klose, M., Leung, D. M., Li, L., Mahowald, N. M., Miller, R. L.,
1058 Obiso, V., Pérez García-Pando, C., Rocha-Lima, A., Wan, J. S., and Whicker, C. A.: Improved
1059 representation of the global dust cycle using observational constraints on dust properties and
1060 abundance, Atmos. Chem. Phys., 21, 8127–8167, https://doi.org/10.5194/acp-21-8127-2021, 2021a.

1061

1062 Kok, J. F., Adebiyi, A. A., Albani, S., Balkanski, Y., Checa-Garcia, R., Chin, M., Colarco, P. R.,
1063 Hamilton, D. S., Huang, Y., Ito, A., Klose, M., Li, L., Mahowald, N. M., Miller, R. L., Obiso, V.,
1064 Pérez García-Pando, C., Rocha-Lima, A., and Wan, J. S.: Contribution of the world's main dust source
1065 regions to the global cycle of desert dust, Atmos. Chem. Phys., 21, 8169–8193,
1066 https://doi.org/10.5194/acp-21-8169-2021, 2021b.

1067

1068 Koren, I., Yoram, J. K., Richard, W., Martin, C. T., Yinon, R., Martins., J. V., and Daniel, R.: The
1069 Bodélé depression: a single spot in the Sahara that provides most of the mineral dust to the Amazon
1070 forest, Environ. Res. Lett., 1, 014005, https://doi.org/10.1088/1748-9326/1/1/014005, 2006.

1071

1072 Kosmopoulos, P.G., Kazadzis, S., El-Askary, H., Taylor, M., Gkikas, A., Proestakis, E., Kontoes, C.,
1073 El-Khayat, M.M.: Earth-Observation-Based Estimation and Forecasting of Particulate Matter Impact
1074 on Solar Energy in Egypt, Remote Sens., 10, 1870, 2018.

1075

1076 Lambert, F., Kug, J.-S., Park, R. J., Mahowald, N., Winckler, G., Abe-Ouchi, A., O'ishi, R.,
1077 Takemura, T., and Lee, J.-H.: The role of mineral-dust aerosols in polar temperature amplification,
1078 Nat. Clim. Change, 3, 487–491, https://doi.org/10.1038/nclimate1785, 2013.

1079

1080 Levy, R. C., Leptoukh, G. G., Kahn, R., Zubko, V., Gopalan, A., and Remer, L. A.: A critical look at
1081 deriving monthly aerosol optical depth from satellite data, IEEE T. Geosci. Remote, 47, 2942–2956,
1082 https://doi.org/10.1109/TGRS.2009.2013842, 2009.

1083

1084 Levy, R. C., Mattoo, S., Munchak, L. A., Remer, L. A., Sayer, A. M., Patadia, F., and Hsu, N. C.:
1085 The Collection 6 MODIS aerosol products over land and ocean, Atmos. Meas. Tech., 6, 2989–3034,
1086 https://doi.org/10.5194/amt-6-2989-2013, 2013.

1087

1088 Li, L., and Sokolik, I.: Analysis of Dust Aerosol Retrievals Using Satellite Data in Central Asia,
1089 Atmosphere, 9, 288, 2018.

1090

1091 Liu, D., Wang, Z., Liu, Z., Winker, D., and Trepte, C.: A height resolved global view of dust aerosols
1092 from the first year CALIPSO lidar measurements, J. Geophys. Res.-Atmos., 113, D16214,
1093 https://doi.org/10.1029/2007JD009776, 2008.

1094
1095

Logothetis, S.-A., Salamalikis, V., Gkikas, A., Kazadzis, S., Amiridis, V., and Kazantzidis, A.: 15-year variability of desert dust optical depth on global and regional scales, Atmos. Chem. Phys., 21, 16499–16529, https://doi.org/10.5194/acp-21-16499-2021, 2021.

Mahowald, N. M. and Luo, C.: A less dusty future?, Geophys. Res.Lett., 30, 1903, https://doi.org/10.1029/2003GL017880, 2003.

Marinou, E., Amiridis, V., Binietoglou, I., Tsikerdekis, A., Solomos, S., Proestakis, E., Konsta, D., Papagiannopoulos, N., Tsekeri, A., Vlastou, G., Zanis, P., Balis, D., Wandinger, U., and Ansmann, A.: Three-dimensional evolution of Saharan dust transport towards Europe based on a 9-year EARLINET-optimized CALIPSO dataset, Atmos. Chem. Phys., 17, 5893-5919, https://doi.org/10.5194/acp-17-5893-2017, 2017.

Marticoréna, B.: Mineral Dust - A key player in the Earth system, chap. Chapter 5: Dust production mechanisms, pp. 93–120, Springer, 2014.

Masoom, A., Kosmopoulos, P., Bansal, A., Gkikas, A., Proestakis, E., Kazadzis, S., Amiridis, V.: Forecasting dust impact on solar energy using remote sensing and modeling techniques, Solar Energy, Vol. 228, 317-332, https://doi.org/10.1016/j.solener.2021.09.033, 2021.

Mazzonia, E., & Vazquez, M.: Desertification in Patagonia. In E. M. Latrubesse (Ed.), Natural hazards and human-exacerbated disasters in Latin America, (Vol. 13, pp. 351–377). Elsevier, https://doi.org/https://doi.org/10.1016/S0928-2025(08)10017-7, 2009.

McConnell, J. R., Aristarain, A. J., Banta, J. R., Edwards, P. R., and Simões, J. C.: 20th-century doubling in dust archived in an Antarctic Peninsula ice core parallels climate change and desertification in South America, Proc. Natl. Acad. Sci. U. S. A., 104, 5743–5748, 2007.

Micklin, P.: The Aral Sea disaster, Annu. Rev. Earth Planet. Sci., 35, 47–72, 2007.

Middleton, N. J.: Dust storms in the Middle East, J. Arid Environ., 10, 83–96, 1986.

Middleton, H. J.: Desert dust hazards: A global review, Aeolian Res., 24, 53–63, 2017.

¶

Middleton, N. J. and Goudie, A. S.: Saharan dust: sources and trajectories, T. I. Brit. Geogr., 26, 165–181, doi:10.1111/1475- 5661.00013, 2001.

Middleton, N.J., Kang, U.: Sand and dust storms: impact mitigation, Sustainability, 9, 1053, https://doi.org/10.3390/su9061053, 2017.

Mitchell, R. M., Forgan, B. W., and Campbell, S. K.: The Climatology of Australian Aerosol, Atmos. Chem. Phys., 17, 5131-5154, https://doi.org/10.5194/acp-17-5131-2017, 2017.

Moran-Zuloaga, D., Ditas, F., Walter, D., Saturno, J., Brito, J., Carbone, S., Chi, X., Hrabě de Angelis, I., Baars, H., Godoi, R. H. M., Heese, B., Holanda, B. A., Lavrič, J. V., Martin, S. T., Ming, J., Pöhlker, M. L., Ruckteschler, N., Su, H., Wang, Y., Wang, Q., Wang, Z., Weber, B., Wolff, S., Artaxo, P., Pöschl, U., Andreae, M. O., and Pöhlker, C.: Long-term study on coarse mode aerosols in the Amazon rain forest with the frequent intrusion of Saharan dust plumes, Atmos. Chem. Phys., 18, 10055-10088, https://doi.org/10.5194/acp-18-10055-2018, 2018.

Nabat, P., Somot, S., Mallet, M., Michou, M., Sevault, F., Driouech, F., Meloni, D., di Sarra, A., Di Biagio, C., Formenti, P., Sicard, M., Léon, J.-F., and Bouin, M.-N.: Dust aerosol radiative effects during summer 2012 simulated with a coupled regional aerosol–atmosphere–ocean model over the Mediterranean, Atmos. Chem. Phys., 15, 3303-3326, https://doi.org/10.5194/acp-15-3303-2015, 2015.

Okin, G. S., Mahowald, N., Chadwick, O. A., and Artaxo, P.: Impact of desert dust on the biogeochemistry of phosphorus in terrestrial ecosystems, Global Biogeochem. Cy., 18, GB2005, https://doi.org/10.1029/2003GB002145, 2004.

O'Neill, N. T., Ignatov, A., Holben, B. N., and Eck, T. F.: The lognormal distribution as a reference for reporting aerosol optical depth statistics; Empirical tests using multi-year, multi-site AERONET Sunphotometer data, Geophys. Res. Lett., 27, 3333–3336, https://doi.org/10.1029/2000GL011581, 2000.

Pease, P. P., Tchakerian, V. P., and Tindale, N. W.: Aerosols over the Arabian Sea: geochemistry and source areas for Aeolian desert dust, J. Arid Environ., 39, 477–496, https://doi.org/10.1006/jare.1997.0368, 1998.

1165 Pérez, C., Nickovic, S., Pejanovic, G., Baldasano, J. M., and Özsoy, E.: Interactive dust-radiation
1166 modeling: A step to improve weather forecasts, J. Geophys. Res., 111, 1–17, 2006.
1167
1168 Pérez García-Pando, C., Stanton, M. C., Diggle, P. J., Trzaska, S., Miller, R. L., Perlwitz, J. P.,
1169 Baldasano, J. M., Cuevas, E., Ceccato, P., Yaka, P., and Thomson, M. C.: Soil Dust Aerosols and
1170 Wind as Predictors of Seasonal Meningitis Incidence in Niger, Environ. Health Perspect., 122, 679–
1171 686, doi:10.1289/ehp.1306640, 2014a.
1172
1173 Pérez García-Pando, C., Thomson, M.C., Stanton, M., Diggle, P., Hopson, T., Pandya, R. and Miller,
1174 R.L.: Meningitis and climate: From science to practice. Earth Perspect., 1, 14, doi:10.1186/2194-
1175 6434-1-14, 2014b.
1176
1177 Peyridieu, S., Chédin, A., Capelle, V., Tsamalis, C., Pierangelo, C., Armante, R., Crevoisier, C.,
1178 Crépeau, L., Siméon, M., Ducos, F., and Scott, N. A.: Characterisation of dust aerosols in the infrared
1179 from IASI and comparison with PARASOL, MODIS, MISR, CALIOP, and AERONET observations,
1180 Atmos. Chem. Phys., 13, 6065-6082, https://doi.org/10.5194/acp-13-6065-2013, 2013.
1181
1182 Piketh, S., Annegarn, H., and Tyson, P.: Lower tropospheric aerosol loadings over South Africa: the
1183 relative contribution of aeolian dust, industrial emissions, and biomass burning, J. Geophys.Res., 104,
1184 1597–1607, 1999.
1185
1186 Prasad, A. K., Singh, S., Chauhan, S., Srivastava, M. K., Singh, R. P., and Singh, R.: Aerosol radiative
1187 forcing over the IndoGangetic plains during major dust storms, Atmos. Environ., 41, 6289–6301,
1188 doi:10.1016/j.atmosenv.2007.03.060, 2007a.
1189
1190 Prasad, A. K. and Singh, R. P.: Changes in aerosol parameters during major dust storm events (2001–
1191 2005) over the Indo-Gangetic Plains using AERONET and MODIS data, J. Geophys. Res.- Atmos.,
1192 112, D09208, https://doi.org/10.1029/2006JD007778, 2007b.
1193
1194 Proestakis, E., Amiridis, V., Marinou, E., Georgoulias, A. K., Solomos, S., Kazadzis, S., Chimot, J.,
1195 Che, H., Alexandri, G., Binietoglou, I., Daskalopoulou, V., Kourtidis, K. A., de Leeuw, G., and van
1196 der A, R. J.: Nine-year spatial and temporal evolution of desert dust aerosols over South and East
1197 Asia as revealed by CALIOP, Atmos. Chem. Phys., 18, 1337-1362, https://doi.org/10.5194/acp-18-
1198 1337-2018, 2018.
1199

Prospero, J. M.: Long-range transport of mineral dust in the global atmosphere: Impact of African dust on the environment of the southeastern United States, P. Natl. Acad. Sci. USA, 96, 3396–3403, 1999.

Prospero, J. M., Collard, F. X., Molinie, J., and Jeannot, A.: Characterizing the annual cycle of African dust transport to the Caribbean Basin and South America and its impact on the environment and air quality, Global Biogeochem. Cy., 28, 757–773, https://doi.org/10.1002/2013gb004802, 2014.

Prospero, J. M., Ginoux, P., Torres, O., Nicholson, S. E., and Gill, T. E.: Environmental characterization of global sources of atmospheric soil dust identified with the Nimbus 7 Total Ozone Mapping Spectrometer (TOMS) absorbing aerosol product, Rev. Geophys., 40, 2-1–2-31, 2002.

Prospero, J. M. and Lamb, P. J.: African droughts and dust transport to the Caribbean: climate change implications, Science, 302,1024–1027, doi:10.1126/science.1089915, 2003.

Querol X., Tobías, A., Pérez, N., Karanasiou, A., Amato, F., Stafoggia, M., Pérez García-Pando, C., Ginoux, P., Forastiere, F., Gumy, S., Mudu, P., Alastuey, A.: Monitoring the impact of desert dust outbreaks for air quality for health studies, Environ Int., 130:104867, doi: 10.1016/j.envint.2019.05.061. Epub 2019 Jun 14. PMID: 31207476; PMCID: PMC6686079, 2019.

Ramaswamy, V.P., Muraleedharan, M., Prakash Babu, C.: Mid-troposphere transport of Middle-East dust over the Arabian Sea and its effect on rainwater composition and sensitive ecosystems over India. Scientific Reports 7, 13676, https://doi.org/10.1038/s41598-017-13652-1, 2017.

Rajot, J. L., Formenti, P., Alfaro, S., Desboeufs, K., Chevaillier, S., Chatenet, B., Gaudichet, A., Journet, E., Marticorena, B., Triquet, S., Maman, A., Mouget, N., and Zakou, A.: AMMA dust experiment: An overview of measurements performed during the dry season special observation period (SOP0) at the Banizoumbou (Niger) supersite, J. Geophys. Res., 113, D00C14, doi:10.1029/2008jd009906, 2008.

Rashki, A., Kaskaoutis, D.G., Francois, P., Kosmopoulos, P.G., Legrand, M.: Dust-storm dynamics over Sistan region, Iran: seasonality, transport characteristics and affected areas, Aeol. Res., 16, 35–48, 2015.

1232   Ridley, D. A., Heald, C. L., Kok, J. F., and Zhao, C.: An observationally constrained estimate of

1233   global dust aerosol optical depth, Atmos. Chem. Phys., 16, 15097–15117,

1234   https://doi.org/10.5194/acp-16-15097-2016, 2016.

1235

1236   Rivera Rivera, N. I., Gill, T. E., Gebhart, K. A., Hand, J. L., Bleiweiss, M. P., and Fitzgerald, R. M.:

1237   Wind modeling of Chihuahuan Desert dust outbreaks, Atmos. Environ., 43(2), 347–354,

1238   doi:10.1016/j.atmosenv.2008.09.069, 2009.

1239

1240   Rodríguez, S., Cuevas, E., Prospero, J. M., Alastuey, A., Querol, X., López-Solano, J., García, M. I.,

1241   and Alonso-Pérez, S.: Modulation of Saharan dust export by the North African dipole, Atmos. Chem.

1242   Phys., 15, 7471-7486, https://doi.org/10.5194/acp-15-7471-2015, 2015.

1243

1244   Rohrmann, A., Heermance, R., Kapp, P., and Cai, F. L.: Wind as the primary driver of erosion in the

1245   Qaidam Basin, China. Earth Planet. Sci. Lett., 374, 1–10, https://doi.org/10.1016/j.epsl.2013.03.011,

1246   2013.

1247

1248   Saiko, T.A., Zonn, I.S.: Irrigation expansion and dynamics of desertification in the circum-aral region

1249   of central Asia, Appl. Geogr., 20, 349–367, 2000.

1250

1251   Sayer, A. M. and Knobelspiesse, K. D.: How should we aggregate data? Methods accounting for the

1252   numerical distributions, with an assessment of aerosol optical depth, Atmos. Chem. Phys., 19, 15023–

1253   15048, https://doi.org/10.5194/acp-19-15023-2019, 2019.

1254

1255   Schepanski, K., Tegen, I., Laurent, B., Heinold, B., and Macke, A.: A new Saharan dust source

1256   activation frequency map derived from MSG-SEVIRI IR channels, Geophys. Res. Lett., 34, L18803,

1257   https://doi.org/10.1029/2007GL030168, 2007.

1258

1259   Schepanski, K., Tegen, I., Todd, M. C., Heinold, B., Bönisch, G., Laurent, B., and Macke, A.:

1260   Meteorological processes forcing Saharan dust emission inferred from MSG-SEVIRI observations of

1261   subdaily dust source activation and numerical models, J. Geophys. Res.-Atmos., 114, D10201,

1262   https://doi.org/10.1029/2008JD010325, 2009.

1263

1264   Schepanski, K., Heinold, B., and Tegen, I.: Harmattan, Saharan heat low, and West African monsoon

1265   circulation: modulations on the Saharan dust outflow towards the North Atlantic, Atmos. Chem.

1266   Phys., 17, 10223-10243, https://doi.org/10.5194/acp-17-10223-2017, 2017.

1267

Shen, H., Abuduwaili, J., Samat, A., Ma, L.: A review on the research of modern aeolian dust in Central Asia, Arab J Geosci., 9:625, 2016.

Sogacheva, L., de Leeuw, G., Rodriguez, E., Kolmonen, P., Georgoulias, A. K., Alexandri, G., Kourtidis, K., Proestakis, E., Marinou, E., Amiridis, V., Xue, Y., and van der A, R. J.: Spatial and seasonal variations of aerosols over China from two decades of multi-satellite observations – Part 1: ATSR (1995–2011) and MODIS C6.1 (2000–2017), Atmos. Chem. Phys., 18, 11389-11407, https://doi.org/10.5194/acp-18-11389-2018, 2018.

Sokolik, I. N. and Toon, O. B.: Direct radiative forcing by anthropogenic airborne mineral aerosols, Nature, 381, 681–683, https://doi.org/10.1038/381681a0, 1996.

Song, Q., Zhang, Z., Yu, H., Ginoux, P., and Shen, J.: Global dust optical depth climatology derived from CALIOP and MODIS aerosol retrievals on decadal timescales: regional and interannual variability, Atmos. Chem. Phys., 21, 13369–13395, https://doi.org/10.5194/acp-21-13369-2021, 2021.

Srivastava, A. K., Tiwari, S., Devara, P. C. S., Bisht, D. S., Srivastava, M. K., Tripathi, S. N., Goloub, P., and Holben, B. N.: Pre-monsoon aerosol characteristics over the Indo-Gangetic Basin: implications to climatic impact, Ann. Geophys., 29, 789-804, https://doi.org/10.5194/angeo-29-789-2011, 2011.

Stanelle, T., Bey, I., Raddatz, T., Reick, C., and Tegen, I.: Anthro- pogenically induced changes in twentieth century mineral dust burden and the associated impact on radiative forcing, J. Geo- phys. Res.-Atmos., 119, 13526–13546, 2014.

Stefanski, R. and Sivakumar, M. V. K.: Impacts of sand and dust storms on agriculture and potential agricultural applications of a SDSWS, IOP Conf. Ser.: Earth Environ. Sci., 7, 012016, doi: 10.1088/1755-1307/7/1/012016, 2009.

Sun, Y., Chen, H., Tada, R., Weiss, D., Lin, M., Toyoda, S., Yan, Y., and Isozaki, Y.: ESR signal intensity and crystallinity of quartz from Gobi and sandy deserts in East Asia and implication for tracing Asian dust provenance, Geochem. Geophy. Geosy., 14, 2615–2627, https://doi.org/10.1002/ggge.20162, 2013.

1300

1301 Tanaka, T. Y. and Chiba, M.: A numerical study of the contributions of dust source regions to the
1302 global dust budget, Global Planet Change, 52, 88–104,
1303 https://doi.org/10.1016/j.gloplacha.2006.02.002,2006.

1304 Tegen, I., Werner, M., Harrison, S., and Kohfeld, K.: Relative im- portance of climate and land use
1305 in determining present and fu- ture global soil dust emission, Geophys. Res. Lett., 31, L05105,
1306 https://doi.org/10.1029/2003GL019216, 2004.

1307 Tegen, I., Heinold, B., Todd, M., Helmert, J., Washington, R., and Dubovik, O.: Modelling soil dust
1308 aerosol in the Bodélé depression during the BoDEx campaign, Atmos. Chem. Phys., 6, 4345-4359,
1309 https://doi.org/10.5194/acp-6-4345-2006, 2006.
1310

1311 Tong, D. Q., Wang, J. X. L., Gill, T. E., Lei, H., and Wang, B. Y.: Intensified dust storm activity and
1312 Valley fever infection in the southwestern United States, Geophys. Res. Lett., 44, 4304–4312,
1313 https://doi.org/10.1002/2017gl073524, 2017.
1314

1315 Tyson, P.D., Garstang, M., Swap, R., Kallberg, P., Edwards, M.: An air transport climatology for
1316 subtropical southern Africa. Int. J. Climatol. 16 (3), 265–291, 1996.
1317

1318 Vickery, K. J., Eckardt, F. D., and Bryant, R. G.: A sub-basin scale dust plume source frequency
1319 inventory for south-ern Africa, 2005–2008, Geophys. Res. Lett., 40, 5274–5279,
1320 doi:10.1002/grl.50968, 2013.
1321

1322 Voss, K. K., and Evan, A. T.: A new satellite-based global climatology of dust aerosol optical depth.
1323 Journal of Applied Meteorology and Climatology, doi:10.1175/jamc-d-19-0194.1, 2020.
1324

1325 Wagener, T., Guieu, C., Losno, R., Bonnet, S., and Mahowald, N.: Revisiting atmospheric dust export
1326 to the Southern Hemisphere ocean: Biogeochemical implications, Glob. Biogeochem. Cy., 22,
1327 GB2006, https://doi.org/10.1029/2007gb002984, 2008.
1328

1329 Washington, R., Todd, M., Middleton, N. J., and Goudie, A. S.: Dust-storm source areas determined
1330 by the total ozone monitoring spectrometer and surface observations, Ann. Assoc. Am. Geogr., 93,
1331 297–313, https://doi.org/10.1111/1467-8306.9302003, 2003.
1332

Washington, R. and Todd, M. C.: Atmospheric controls on mineral dust emission from the Bodélé depression, Chad: The role of the low level jet, Geophys. Res. Lett., 32, L17701, https://doi.org/10.1029/2005GL023597, 2005.

Washington, R., Bouet, C., Cautenet, G., Mackenzie, E., Ashpole, I., Engelstaedter, S., Lizcano, G., Henderson, G. M., Schepanski, K., and Tegen, I.: Dust as a tipping element: the Bodélé Depression, Chad, P. Natl. Acad. Sci. USA, 106, 20564–20571, doi:10.1073/pnas.0711850106, 2009.

Weinzierl, B., Sauer, D., Minikin, A., Reitebuch, O., Dahlkotter, F., Mayer, B., Emde, C., Tegen, I., Gasteiger, J., Petzold, A., Veira, A., Kueppers, U., and Schumann, U.: On the visibility of airborne volcanic ash and mineral dust from the pilot's perspective in flight, Phys Chem Earth, 45-46, 87-102, 10.1016/j.pce.2012.04.003, 2012.

Winker, D. M., Vaughan, M. A., Omar, A., Hu, Y., Powell, K. A., Liu, Z., Hunt, W. H. and Young, S. A.: Overview of the CALIPSO Mission and CALIOP Data Processing Algorithms, J. Atmos. Oceanic Technol., 26(11), 2310–2323, doi:10.1175/2009JTECHA1281.1, 2009.

Yu, H. B., Chin, M., Winker, D. M., Omar, A. H., Liu, Z. Y., Kittaka, C., and Diehl, T.: Global view of aerosol vertical distributions from CALIPSO lidar measurements and GOCART simulations: Regional and seasonal variations, J. Geophys. Res.-Atmos., 115, D00H30, https://doi.org/10.1029/2009jd013364, 2010.

Yu, H. B., Chin, M., Yuan, T. L., Bian, H. S., Remer, L. A., Prospero, J. M., Omar, A., Winker, D., Yang, Y. K., Zhang, Y., Zhang, Z. B., and Zhao, C.: The fertilizing role of African dust in the Amazon rainforest: A first multiyear assessment based on data from Cloud-Aerosol Lidar and Infrared Pathfinder Satellite Observations, Geophys. Res. Lett., 42, 1984–1991, https://doi.org/10.1002/2015gl063040, 2015.

Yu, H., Remer, L. A., Chin, M., Bian, H., Kleidman, R. G., and Diehl, T.: A satellite-based assessment of transpacific transport of pollution aerosol, J. Geophys. Res.-Atmos., 113, D14S12, https://doi.org/10.1029/2007JD009349, 2008.

Yu, Y., Kalashnikova, O. V., Garay, M. J., and Notaro, M.: Climatology of Asian dust activation and transport potential based on MISR satellite observations and trajectory analysis, Atmos. Chem. Phys., 19, 363-378, https://doi.org/10.5194/acp-19-363-2019, 2019.

1368

1369   Yu, Y., Notaro, M., Kalashnikowa, O., Garay, M.: Climatology of summer Shamal wind in the
1370   Middle East, J. Geophys. Res.-Atmos. 121 (1), 289–305, 2016.

1371

1372   Yu, Y., Notaro, M., Liu, Z., Kalashnikova, O., Alkolibi, F., Fadda, E., and Bakhrjy, F.: Assessing
1373   temporal and spatial variations in atmospheric dust over Saudi Arabia through satellite, radiometric,
1374   and   station   data,   J.   Geophys.   Res.-Atmos.,   118,   13253–   13264,
1375   https://doi.org/10.1002/2013JD020677, 2013.

1376

1377   Yu, Y., Kalashnikova, O. V., Garay, M. J., Lee, H., Choi, M., Okin, G. S., Yorks, J. E., Campbell, J.
1378   R., and Marquis, J.: A global analysis of diurnal variability in dust and dust mixture using CATS
1379   observations, Atmos. Chem. Phys., 21, 1427–1447, https://doi.org/10.5194/acp-21-1427-2021, 2021.

1380

1381   Xi, X. and Sokolik, I. N.: Seasonal dynamics of threshold friction velocity and dust emission in
1382   Central Asia, J. Geophys. Res. Atmos., 120(4), 1536–1564, doi:10.1002/2014JD022471, 2015.

1383

1384   Zender, C. S., Huisheng, B., and Newman, D.: Mineral Dust Entrainment and Deposition (DEAD)
1385   model: Description   and   1990s   dust   climatology,   J.   Geophys.   Res.,   108,   4416,
1386   https://doi.org/10.1029/2002JD002775, 2003.

1387
1388
1389
1390
1391
1392
1393
1394
1395
1396
1397
1398
1399
1400
1401

1402 **Table 1:** Annual and seasonal DOD averages, representative for the period 2003-2017, along with the associated
1403 uncertainty. The first three rows refer to the whole globe (GLB), the global land (GLB-land) and global ocean (GLB-
1404 ocean). In the fourth and fifth line are given the results for N. Hemisphere (NHE) and S. Hemisphere (SHE) DODs
1405 whereas in the rest 17 entries the corresponding results for selected subregions (denoted with colored rectangles in Fig. 7
1406 in Gkikas et al. (2021)) are given.

REGION	ANNUAL	DJF	MAM	JJA	SON
GLB	0.032 ± 0.003	0.025 ± 0.004	0.043 ± 0.005	0.040 ± 0.005	0.022 ± 0.004
GLB-land	0.070 ± 0.005	0.063 ± 0.008	0.104 ± 0.011	0.083 ± 0.010	0.049 ± 0.007
GLA-ocean	0.019 ± 0.002	0.015 ± 0.003	0.026 ± 0.003	0.023 ± 0.003	0.012 ± 0.003
NHE	0.056 ± 0.004	0.043 ± 0.005	0.085 ± 0.009	0.071 ± 0.008	0.036 ± 0.005
SHE	0.008 ± 0.001	0.010 ± 0.003	0.008 ± 0.002	0.006 ± 0.002	0.008 ± 0.003
BOD	0.533 ± 0.009	0.483 ± 0.018	0.614 ± 0.020	0.603 ± 0.017	0.451 ± 0.013
GOB	0.092 ± 0.007	0.074 ± 0.010	0.189 ± 0.023	0.078 ± 0.010	0.056 ± 0.005
CAS	0.126 ± 0.007	0.084 ± 0.012	0.158 ± 0.016	0.144 ± 0.011	0.100 ± 0.007
NME	0.227 ± 0.006	0.120 ± 0.009	0.319 ± 0.016	0.271 ± 0.011	0.186 ± 0.009
SUS	0.018 ± 0.001	0.009 ± 0.002	0.033 ± 0.005	0.021 ± 0.003	0.010 ± 0.001
TAK	0.246 ± 0.020	0.114 ± 0.015	0.504 ± 0.047	0.259 ± 0.030	0.130 ± 0.018
THA	0.198 ± 0.007	0.086 ± 0.006	0.291 ± 0.013	0.424 ± 0.033	0.109 ± 0.006
WSA	0.302 ± 0.006	0.199 ± 0.008	0.362 ± 0.015	0.418 ± 0.016	0.237 ± 0.009
EAS	0.077 ± 0.005	0.072 ± 0.014	0.130 ± 0.012	0.056 ± 0.010	0.048 ± 0.006
ENP	0.020 ± 0.002	0.011 ± 0.002	0.047 ± 0.005	0.017 ± 0.004	0.013 ± 0.002
ETA	0.146 ± 0.007	0.109 ± 0.011	0.169 ± 0.015	0.202 ± 0.015	0.093 ± 0.009
GOG	0.309 ± 0.021	0.417 ± 0.032	0.416 ± 0.066	0.064 ± 0.021	0.100 ± 0.022
MED	0.081 ± 0.003	0.052 ± 0.008	0.106 ± 0.009	0.096 ± 0.006	0.066 ± 0.005
SME	0.250 ± 0.008	0.154 ± 0.009	0.318 ± 0.016	0.394 ± 0.020	0.166 ± 0.008
SSA	0.326 ± 0.013	0.309 ± 0.015	0.494 ± 0.041	0.241 ± 0.054	0.199 ± 0.020
WNP	0.028 ± 0.002	0.017 ± 0.003	0.064 ± 0.008	0.023 ± 0.006	0.018 ± 0.002
WTA	0.035 ± 0.003	0.006 ± 0.002	0.035 ± 0.005	0.090 ± 0.009	0.017 ± 0.004

1407
1408
1409
1410
1411
1412
1413
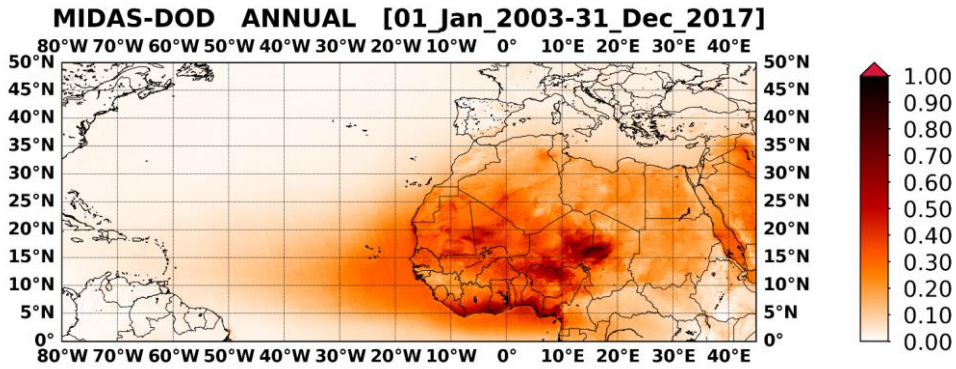
1414

1415 **Figure 1:** Geographical distribution of the MIDAS annual DOD at 550nm, representative for the period 1 January 2003
1416 – 31 December 2017, over North Africa, the Tropical Atlantic Ocean and the broader Mediterranean basin.

1417
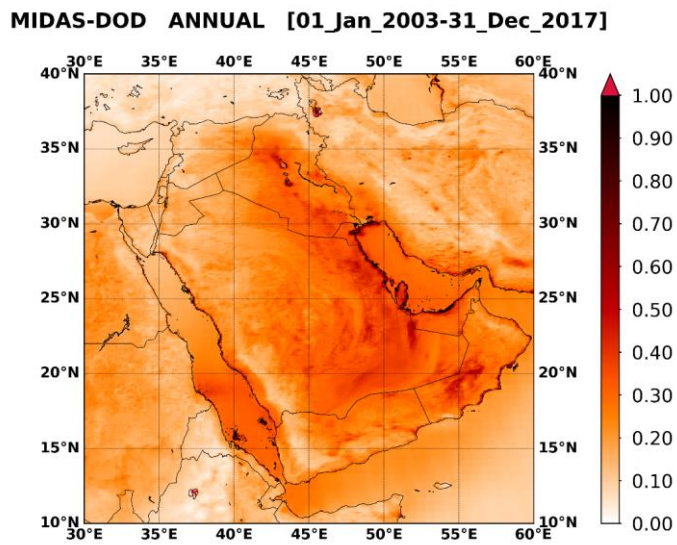
1418
1419 **Figure 2:** As in Figure 1 but for the broader area of the Middle East.
1420

MIDAS-DOD ANNUAL [01_Jan_2003-31_Dec_2017]
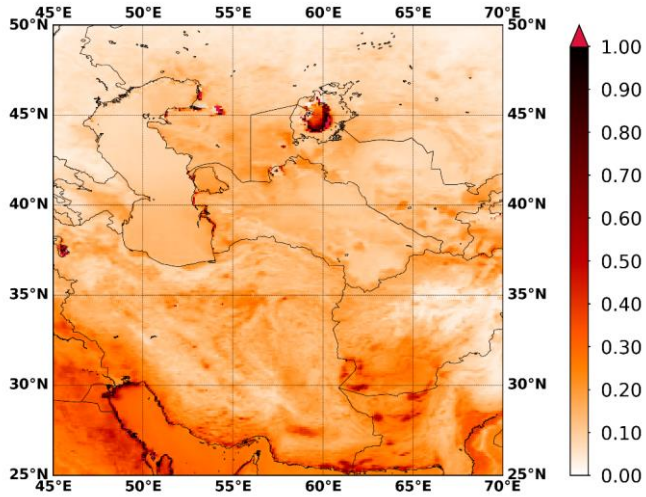
1421
1422   **Figure 3:** As in Figure 1 but for central and southwestern Asia.
1423

MIDAS-DOD ANNUAL [01_Jan_2003-31_Dec_2017]
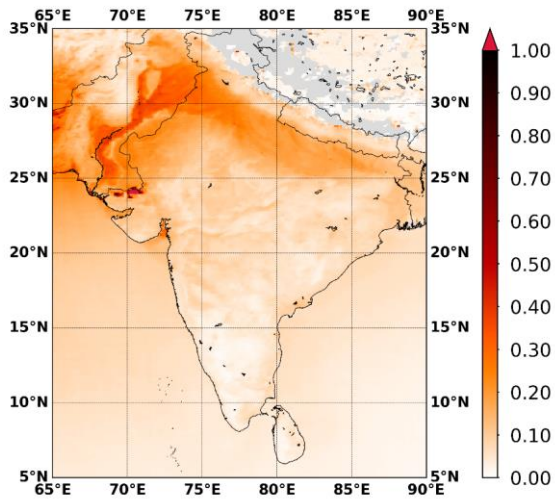
1424
1425   **Figure 4:** As in Figure 1 but for the Indian subcontinent.
1426
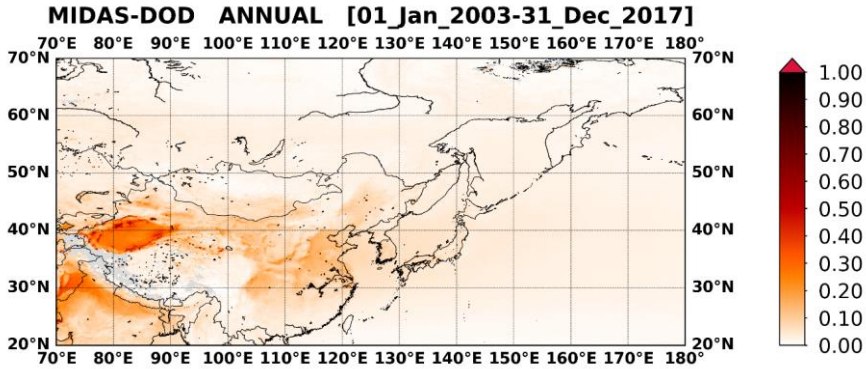
1427
1428 **Figure 5:** As in Figure 1 but for East Asia and the North Pacific Ocean.
1429
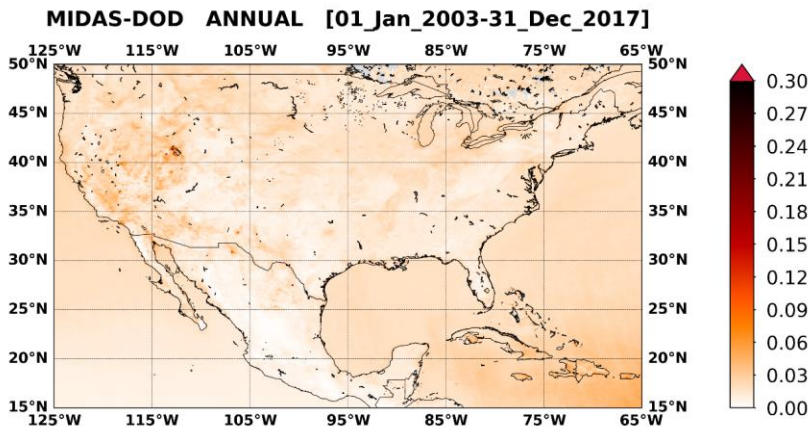
1430
1431 **Figure 6:** As in Figure 1 but for North America.
1432
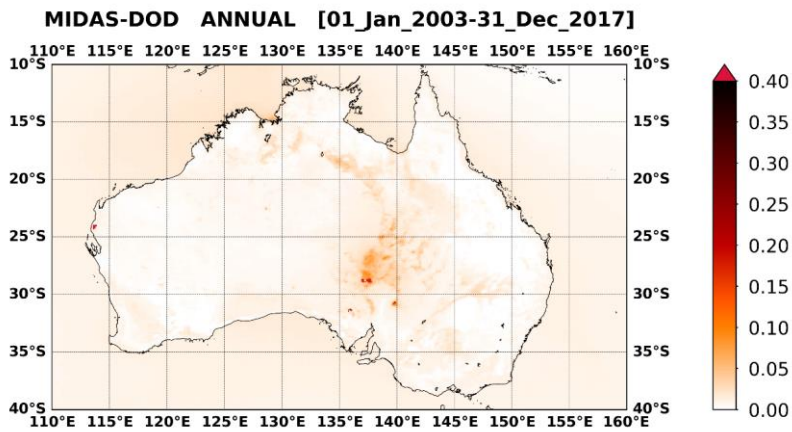
1433
1434 **Figure 7:** As in Figure 1 but for Australia.
1435

1436

MIDAS-DOD   ANNUAL   [01_Jan_2003-31_Dec_2017]
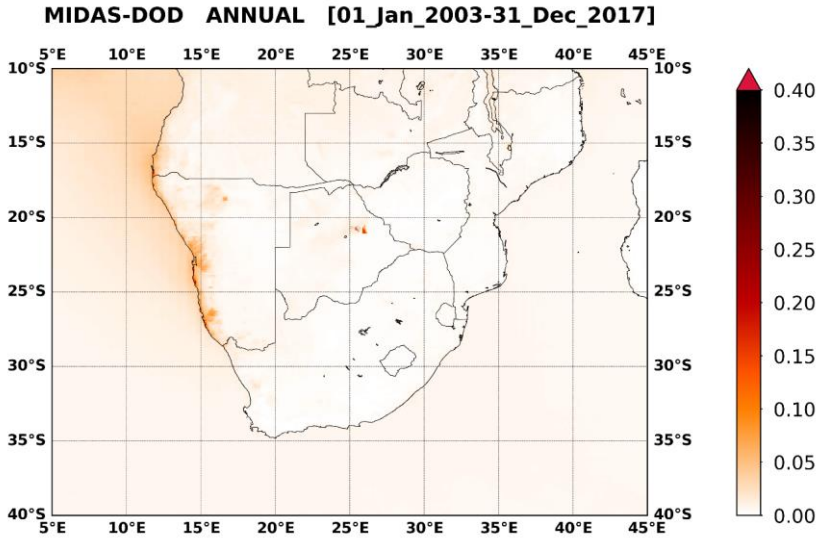
1437
1438   **Figure 8:** As in Figure 1 but for Southern Africa.
1439

MIDAS-DOD   ANNUAL   [01_Jan_2003-31_Dec_2017]
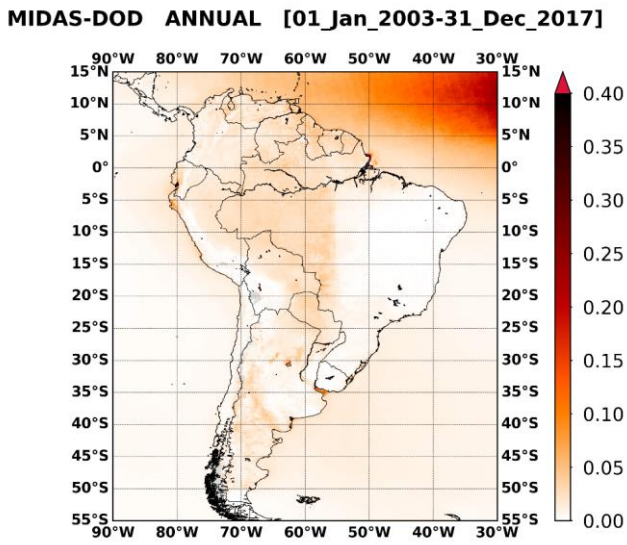
1440
1441   **Figure 9:** As in Figure 1 but for South America.
1442
1443
1444
1445
1446
1447
1448
1449
1450
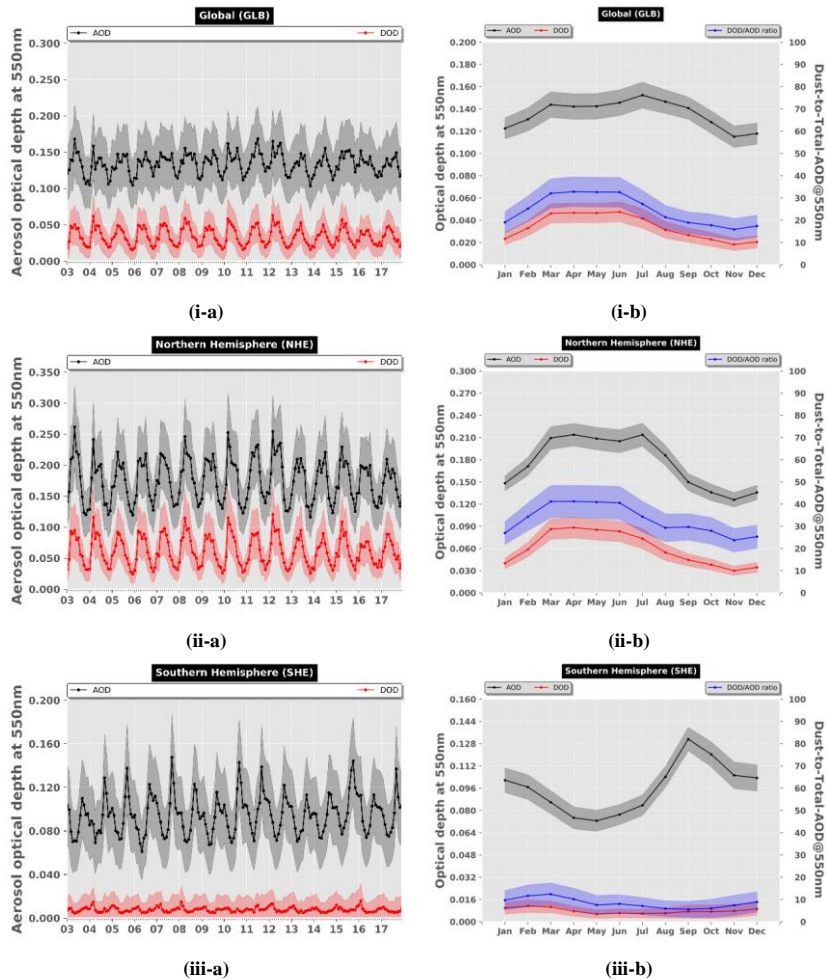
Figure 10: Inter-annual **(-a)** and intra-annual **(-b)** variability, representative for the period 2007 – 2016, of monthly MODIS AOD_{550nm} (black curve) and DOD_{550nm} (red curve) regionally averaged for: **(i)** the whole globe (GLB), **(ii)** the Northern Hemisphere (NHE) and **(iii)** the Southern Hemisphere (SHE). The blue curves in the intra-annual plots depict the dust-to-total AOD_{550nm} ratio (expressed in percentage; right y-axis). The shaded areas correspond to the total uncertainty.
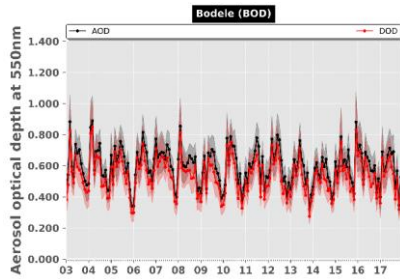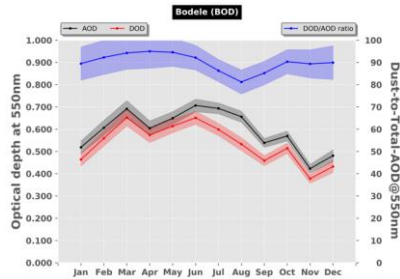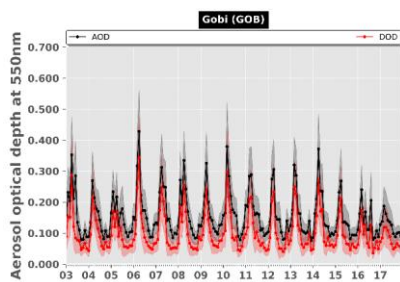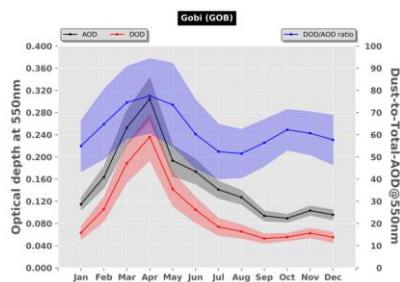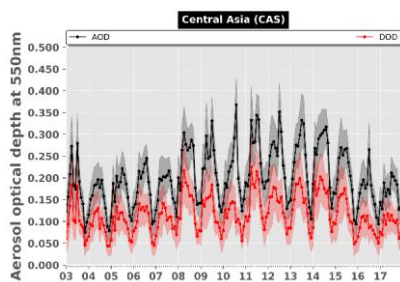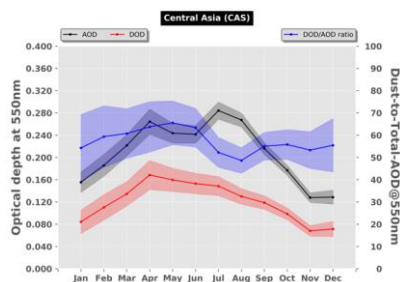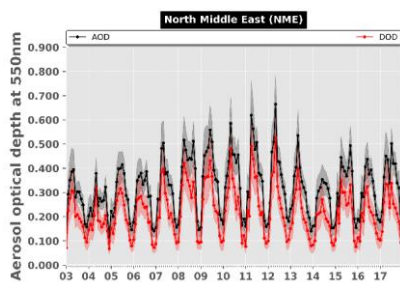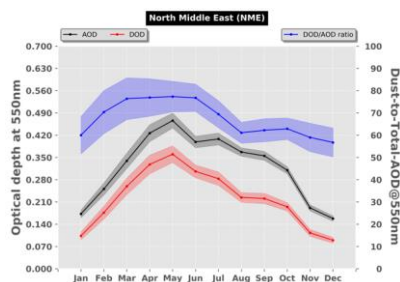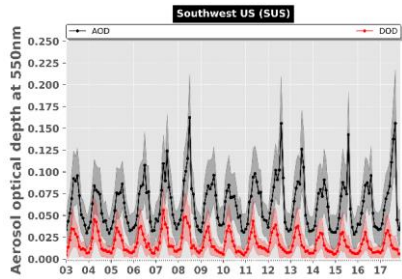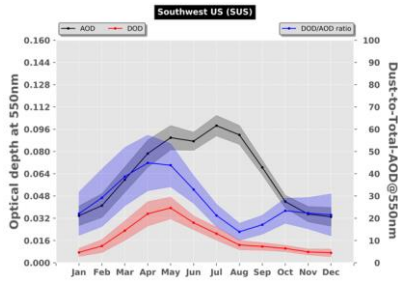
(v-a) **(v-b)**
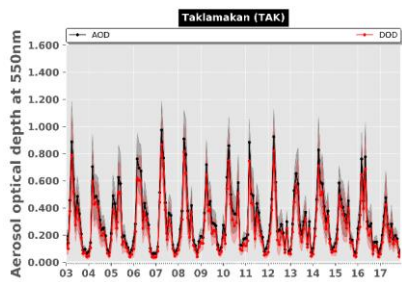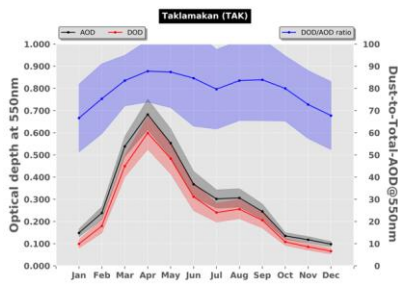
(vi-a) **(vi-b)**
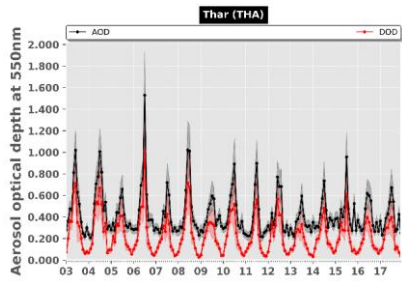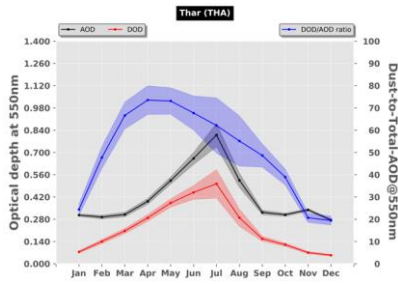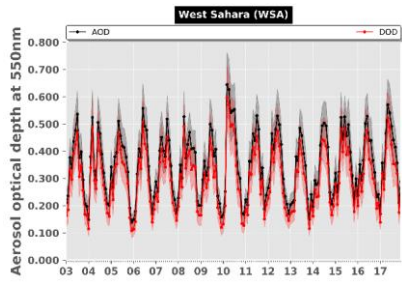
(vii-a) **(vii-b)**
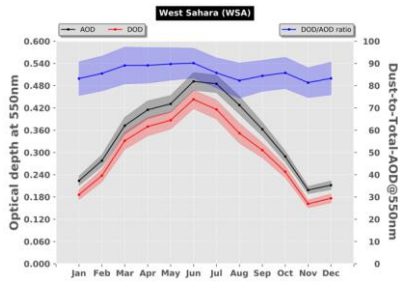
(viii-a) **(viii-b)**
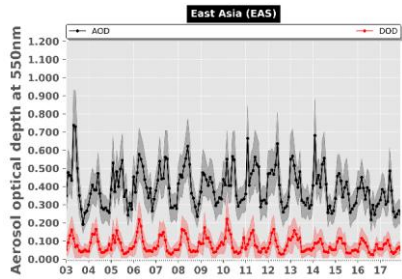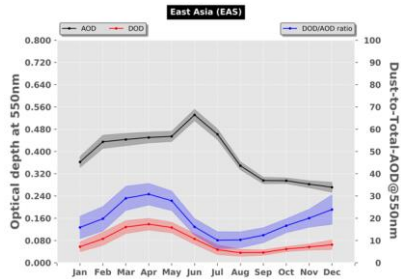
(ix-a)   **(ix-b)**
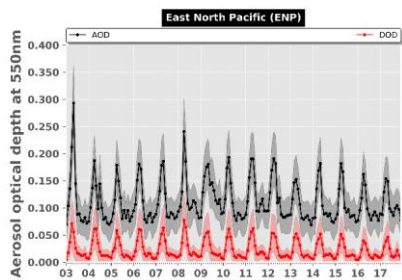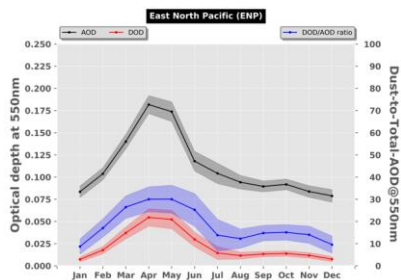
(x-a)   **(x-b)**
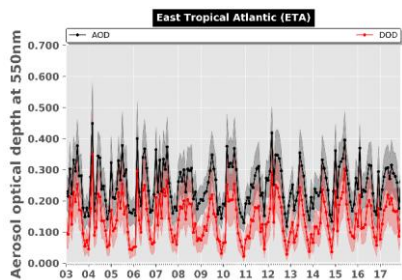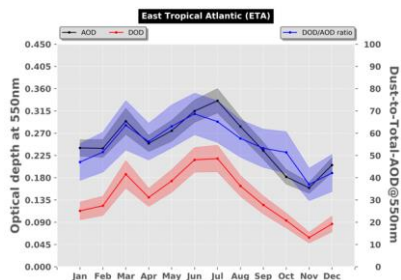
(xi-a)   **(xi-b)**
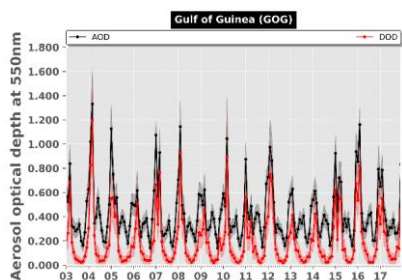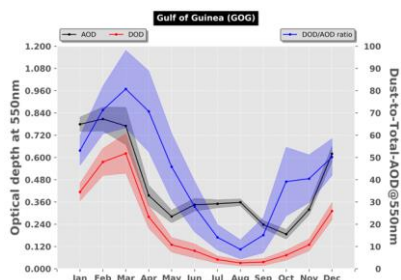
(xii-a)   **(xii-b)**
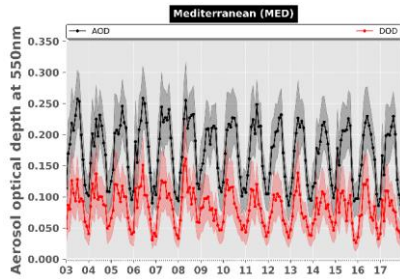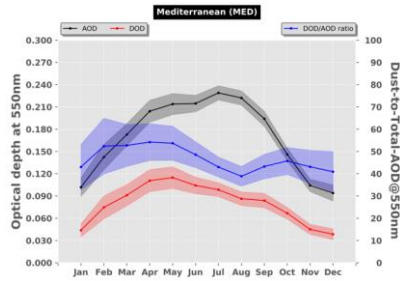
(xiii-a)   **(xiii-b)**
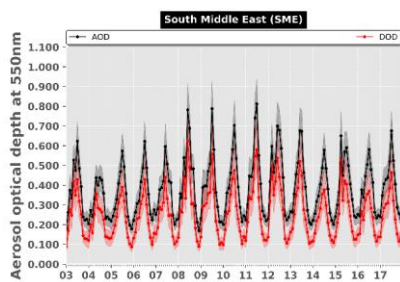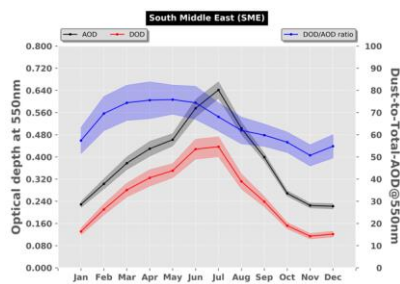
(xiv-a)   **(xiv-b)**

(xv-a)   **(xv-b)**

(xvi-a)   **(xvi-b)**

(xvii-a)   **(xvii-b)**
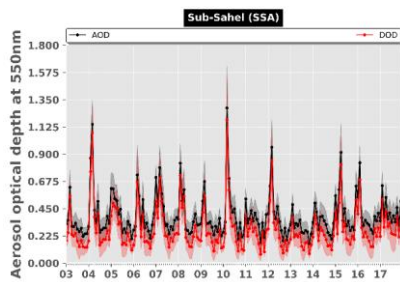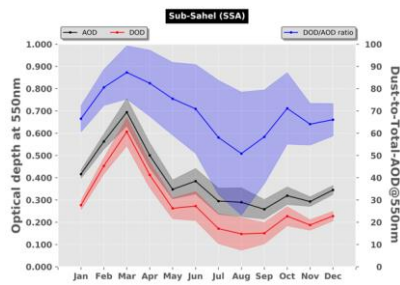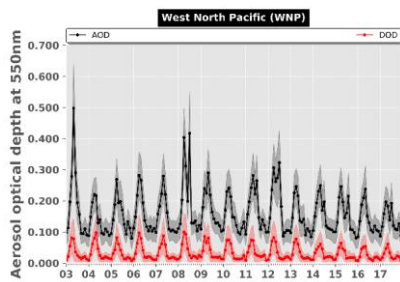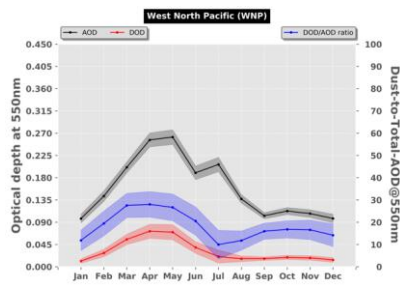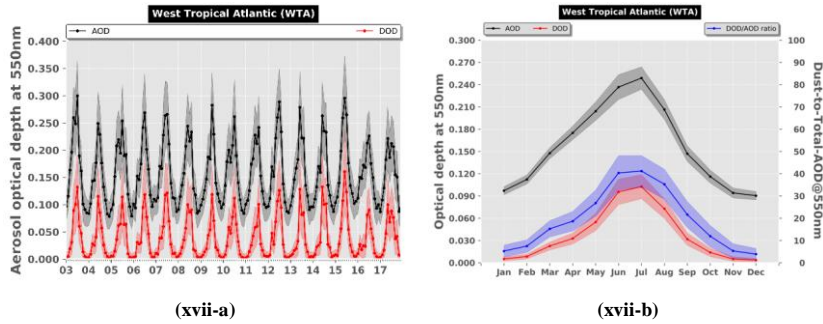
Figure 11: Inter-annual **(-a)** and intra-annual **(-b)** variability, representative for the period 2003 – 2017, of monthly MODIS AOD$_{550nm}$ (black curve) and DOD$_{550nm}$ (red curve) regionally averaged for: **(i)** Bodélé Depression (BOD), **(ii)** Gobi Desert (GOB), **(iii)** Central Asia (CAS), **(iv)** North Middle East (NME), **(v)** southwest United States (SUS), **(vi)** Taklamakan Desert (TAK), **(vii)** Thar Desert (THA), **(viii)** West Sahara (WSA), **(ix)** East Asia (EAS), **(x)** East North Pacific (ENP), **(xi)** East Tropical Atlantic (ETA), **(xii)** Gulf of Guinea (GOG), **(xiii)** Mediterranean (MED), **(xiv)** South Middle East (SME), **(xv)** Sub-Sahel (SSA), **(xvi)** West North Pacific (WNP) and **(xvii)** West Tropical Atlantic (WTA). The shaded areas in the inter and intra-annual plots correspond to the total uncertainty. The blue curves in the intra-annual plots represent the percentage contribution of dust optical depth (DOD) to the aerosol optical depth (AOD).
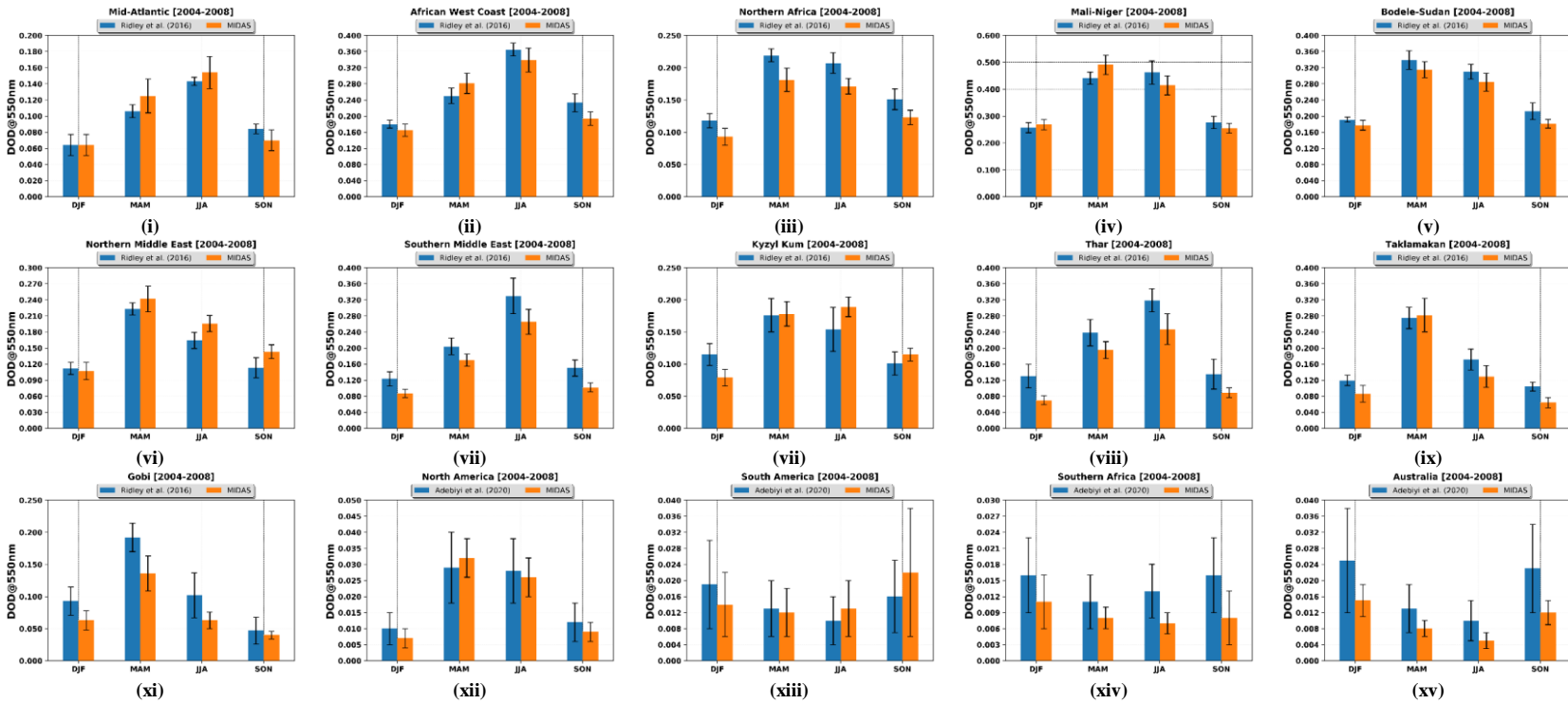
Figure 12: Seasonal DODs, representative for the period 2004 – 2008, based on the MIDAS dataset (orange bars), Ridley et al. (2016) (blue bars) and Adebiyi et al. (2020) (blue bars), for 15 regions (their names are given at the top of each plot) defined in Kok et al. (2021a) (see Table 2). The error bars represent the estimated uncertainties. From i to xi, the blue bars correspond to the Ridley et al. (2016) results whereas for the remaining regions MIDAS DODs are compared against the corresponding levels obtained by Adebiyi et al. (2020).